nature communications

Article

https://doi.org/10.1038/s41467-025-58568-x

Preclinical concept studies showing advantage of an inhaled anti-CTGF/CCN2 protein for pulmonary fibrosis treatment

Received: 25 January 2024

Accepted: 20 March 2025

Published online: 05 April 2025

Check for updates

Vanessa Neiens[1], Eva-Maria Hansbauer[1], Thomas J. Jaquin[1], Janet K. Peper-Gabriel[1], Poornima Mahavadi[2,3], Mark E. Snyder[4,5,6], Maximilian J. Grill[7], Cornelia Wurzenberger[1], Antonio Konitsiotis[1], Adriana Estrada-Bernal[8], Kristina Heinig[1], Athanasios Fysikopoulos[1], Nicolas Schwenck[1], Stefan Grüner[1], Denis Bartoschek[1], Theresia Mosebach[1], Sandra Kerstan[1], Joe Wrennall[9], Marleen Richter[1], Kentaro Noda[10], Konrad Hoetzenecker[11], Janette K. Burgess[12,13], Robert Tarran[9], Claudia Wurzenberger[1], Karl-Robert Wichmann[7], Jonas Biehler[7], Kei W. Müller[7], Andreas Guenther[2,3,14,15,16], Oliver Eickelberg[8], Mary F. Fitzgerald[1], Shane A. Olwill[1,17], Gabriele Matschiner[1,17] & Marina Pavlidou[1,17]

Inhaled therapeutics have high potential for the treatment of chronic respiratory diseases of high unmet medical need, such as idiopathic pulmonary fibrosis (IPF). Preclinical and early clinical evidence show that cellular communication network factor 2 (CCN2), previously called connective tissue growth factor (CTGF), is a promising target for the treatment of IPF. In recent phase 3 clinical trials, however, systemic CCN2 inhibition failed to demonstrate a clinically meaningful benefit. Here, we present the preclinical profile of the inhaled anti-CCN2 Anticalin® protein PRS-220. Our study demonstrates that efficient pulmonary delivery directly translates into superior efficacy in relevant models of pulmonary fibrosis when compared to systemic CCN2 inhibition. Moreover, we present a holistic approach for the preclinical characterization of inhaled PRS-220 from state-of-the art in vitro and in vivo models to novel human ex vivo and in silico models, highlighting the advantage of inhaled drug delivery for treatment of respiratory disease.

Inhaled pulmonary drug delivery for the treatment of respiratory diseases offers multiple advantages over systemic therapies. The drug is directly delivered to the site of the disease increasing the local lung exposure, which can translate into better efficacy. This also enables a lower dose and thus reducing or completely avoiding systemic drug exposure and potential systemic side effects[1]. Inhaled pirfenidone, for example, showed the potential for a better efficacy at lower doses and caused fewer side effects in a clinical study in idiopathic pulmonary fibrosis (IPF) patients when compared to oral pirfenidone, the current standard of care for the treatment of IPF that is often discontinued by patients due to side effects[2,3]. In addition, inhaled therapies are non-invasive alternatives to drugs given via the intravenous or subcutaneous route and can be self-administered leading to potentially higher patient adherence and convenience[4].

Despite the possible advantages of inhaled therapies, the development of inhaled drugs, and especially inhaled biologics, is challenged by drug instability during the aerosolization process, inefficient drug delivery and the lack of suitable models required to analyze their

A full list of affiliations appears at the end of the paper. e-mail: marinapavlidou5@gmail.com

efficacy, lung biodistribution and exposure[5,6]. In clinical development, drug exposure and target engagement in the lung can only be measured indirectly via systemic markers for target engagement or by using invasive methods including sampling of bronchoalveolar lavage or lung biopsies posing a high risk for patients[7]. Taken together, these limitations complicate the prediction of clinical dosing required for optimal efficacy and maximally reduced systemic side-effects and therefore require a detailed understanding of the preclinical drug profile.

Anticalin® proteins are engineered proteins derived from lipocalins, a class of low molecular weight proteins that are abundantly expressed in human tissues and body fluids[8–11].Due to their small size (~18–20 kDa) and highly robust tertiary structure, Anticalin proteins are particularly well-suited for inhalative delivery[12]. Characteristically for biologics, they can achieve specific high-affinity targeting providing the additional benefit of reduced off-target side effects. PRS-220 is an inhaled Anticalin protein targeting cellular communication network factor 2 (CCN2) designed for the treatment of IPF and other fibrotic lung diseases.

IPF is a chronic and ultimately fatal lung disease characterized by progressive scarring of interstitial lung tissue as a consequence of dysregulated wound healing[13]. The unmet medical need for well tolerated and effective therapies is very high due to the poor prognosis for patients and limited benefits conferred by current standard of care, nintedanib and pirfenidone[14]. CCN2, also known as connective tissue growth factor (CTGF), is a member of the CCN family of matricellular proteins[15,16]. Interacting with several different ligands such as cell surface receptors (e.g integrins), cytokines, growth factors (e.g. transforming growth factor β (TGF-β)) and extracellular matrix proteins, CCN2 serves as communication hub and plays important roles in various fundamental cellular processes including proliferation, differentiation, adhesion, angiogenesis, extracellular matrix turnover and wound healing[17]. CCN2 has also been identified as a driver of pathological conditions such as cancer and fibrotic tissue remodeling of the lung, heart, kidney, liver and skin, where CCN2 has been found to be over-expressed in tissues from patients[17–22]. In IPF patients, CCN2 protein levels are increased in different compartments of the lung tissue, including fibroblasts, alveolar and bronchial epithelial cells among others[18,23,24]. In addition, overexpression of CCN2 in the lung has been shown to trigger fibrotic tissue remodeling in vivo[25,26]. In preclinical models, CCN2 is also found upregulated in fibrotic lung tissue and targeting CCN2 by neutralizing agents or genetic approaches attenuated fibrosis showing the suitability of CCN2 as therapeutic target for the treatment of pulmonary fibrosis[22,27–30]. CCN2 blockade by Fibrogen's systemically administered monoclonal antibody pamrevlumab was shown to reduce the lung function decline in patients with IPF in a phase 2 study[31]. Surprisingly, results were not reproducible in a larger population during phase 3, leading to discontinuation of the program[32]. Of note, pulmonary delivery of inhibitors to target CCN2 directly in the lung may be a more promising approach when compared to systemic delivery as demonstrated by preclinical data showing attenuation of fibrotic lung remodeling by local CCN2 targeting in the lung[28,33,34]. In addition, tissue-specific silencing of CCN2 was also shown to attenuate fibrosis in other organs and supports the concept of local CCN2 targeting for effective attenuation of fibrosis[35–37].

Here, we describe the preclinical profile of PRS-220 highlighting that local CCN2 targeting has the potential to overcome the limitations that arise from systemic targeting such as limited tissue penetration. Using a toolbox of healthy and disease-state animal and human models, we thoroughly characterized the lung delivery, lung biodistribution and deposition, as well as efficacy of the inhaled CCN2 inhibitor PRS-220. Our study serves as a case study for preclinical characterization of an inhaled drug candidate. With optimization of existing technologies and development of novel models we aim to expand the portfolio of translatable, human disease-relevant preclinical models to support early de-risking and in-depth characterization of pulmonary drug delivery.

Results

Generation and characterization of the CCN2-specific Anticalin protein PRS-220

PRS-220 was identified by phage display selection using a naive neutrophil gelatinase-associated lipocalin (NGAL)-based Anticalin library followed by one round of targeted optimization to further increase stability and affinity towards CCN2 (Fig. 1a). PRS-220 binds to recombinant CCN2 with a K_D of 0.06 nM ± 0.01 nM as measured by surface plasmon resonance (SPR) and with an EC_{50} of 0.39 nM ± 0.06 nM as measured by enzyme-linked immunosorbent assay (ELISA) (Fig. 1b). PRS-220 is specific to the N-terminal fragment of CCN2 consisting of the insulin-like growth factor binding protein (IGFBP) domain and the von Willebrand type C repeats (vWC) domain, while it does not bind to other members of the CCN (cellular communication network factor) family (Fig. 1b and Supplementary Fig. 1a). In addition, PRS-220 dissociates 169-fold more slowly from CCN2 and binds with 364-fold higher affinity to CCN2 than the clinically tested anti-CCN2 antibody pamrevlumab (Supplementary Fig. 1b) while sharing an overlapping epitope with pamrevlumab as shown by displacement of CCN2 from immobilized pamrevlumab in a competition electrochemiluminescence assay (ECLA) format (Fig. 1c, d).

To confirm that PRS-220 targets CCN2 expressed by disease-relevant myofibroblasts, we tested binding of PRS-220 in a physiological setting by stimulating normal human lung fibroblasts (NHLF) with transforming growth factor β1 (TGF-β1) to induce myofibroblast differentiation and overexpression of CCN2 (Supplementary Fig. 1c). Using immunofluorescence staining of PRS-220 and an NGAL scaffold negative control, we observed a specific and dose-dependent signal increase for PRS-220 specifically in TGF-β1 activated myofibroblasts confirming a dose-dependent targeting of CCN2 that is expressed by myofibroblasts (Supplementary Fig. 1d, e).

PRS-220 is suitable for pulmonary delivery via nebulization

The stability of a drug candidate upon aerosolization is an essential requirement for the development of an inhaled biotherapeutic. We therefore performed a comprehensive assessment of the nebulization performance of PRS-220. PRS-220 was nebulized using the vibrating mesh nebulizer, eFlow® Nebulizer System (PARI), and the generated aerosol was collected in glass vials for analysis with a range of analytical methods to assess biophysicochemical stability and potency. No significant changes were observed between the reference and the post-nebulized samples indicating that the stress of the nebulization did not influence the product quality of PRS-220 (Table 1).

Aerodynamic properties of the aerosol were measured to ensure efficient delivery of PRS-220 to the disease-relevant areas of the airways, which is predominantly driven by the particle size distribution of the aerosol. Only particles with an aerodynamic diameter <5 μm will reach the proximal and distal parts of the lung while larger particles are predominantly deposited in the oropharynx and trachea and are swallowed[38]. Next generation cascade impactor data generated with a formulation of PRS-220 using three identical nebulizer devices showed particle size distributions with mass median aerodynamic diameters (MMAD) between 3.7 μm and 4.2 μm and a geometric standard deviation of 1.5–1.7. These particle size distributions resulted in a fine particle fraction, representing the percentage of mass in particles <5 μm in diameter, between 65% and 77% depending on the device (Table 2). The delivered dose, measured at a breathing simulator, was 57% to 63% of the nominal dose. In conclusion, PRS-220 can be formulated across different concentrations and devices (Table 2, Supplementary Table 1), to achieve aerodynamic properties similar to formulations containing small molecule active pharmaceutical ingredients (API). These aerodynamic properties allow efficient pulmonary delivery of PRS-220 to the desired site of CCN2 expressing lung tissue to achieve optimal target engagement.

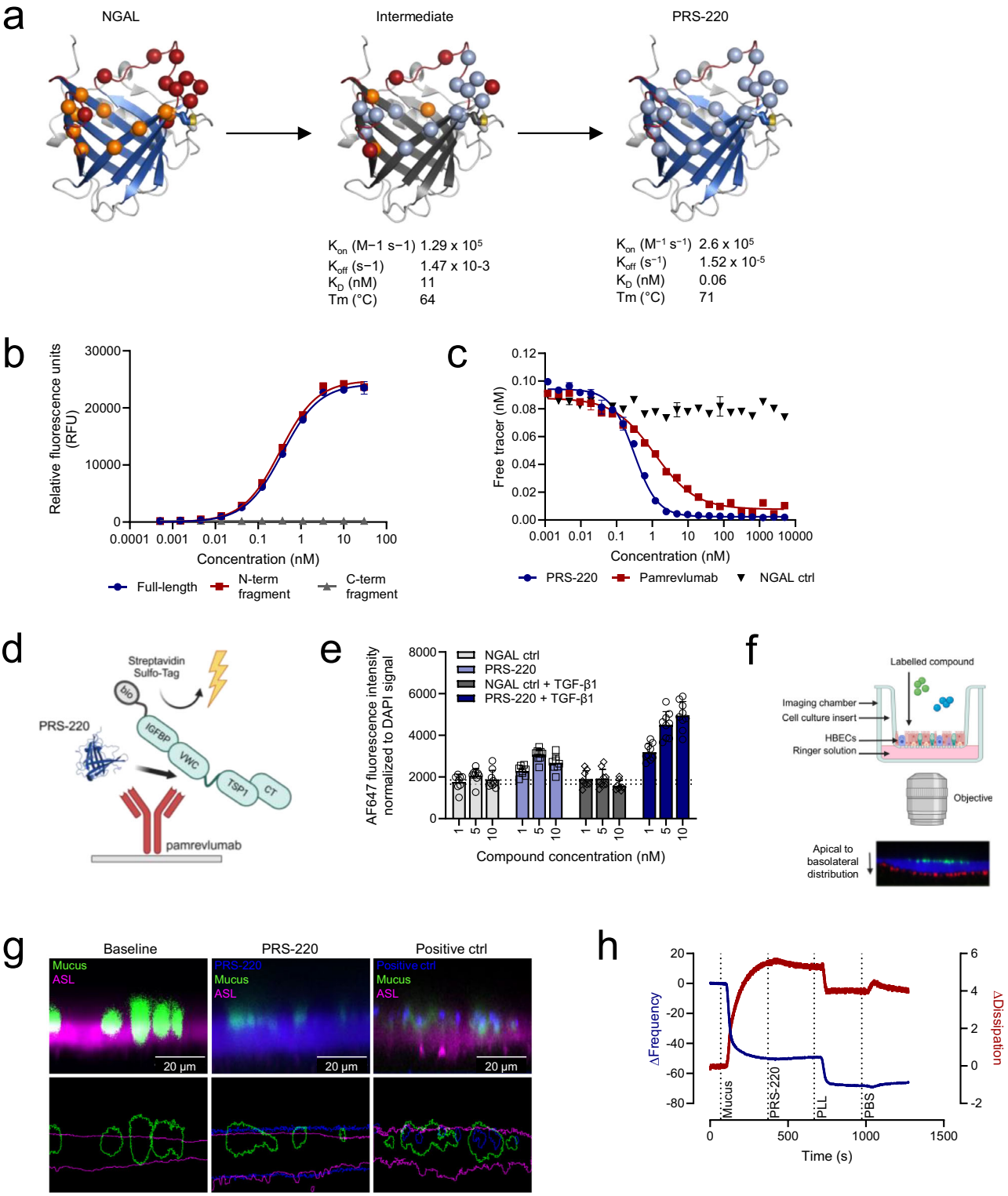

Next, we tested mucus interaction and penetration to ensure that inhaled PRS-220 can permeate the epithelial lining fluid and mucus layer to reach its target CCN2 in the lung tissue. Imaging of fluorescently labeled PRS-220, which was added to the apical surface of bronchial epithelial cells cultured at the air-liquid interface and secreting high levels of mucus, showed that PRS-220 quickly penetrates the mucus layer and distributes evenly in the airway surface liquid of the lung epithelium (Fig. 1f, g). Moreover, using Quartz Crystal Microbalance with Dissipation (QCMD) monitoring, we observed no changes in mucus mass or mucus hydration when adding PRS-220, which is typically observed for compounds interacting with mucins such as poly-L-lysine used as a positive control in this experiment (Fig. 1h). Thus PRS-220 does not interact with mucins as measured by QCMD.

Pulmonary delivery of PRS-220 achieves more efficient penetration of fibrotic lung tissue when compared to a systemic antibody

To characterize the drug distribution in the in vivo setting, we compared in mice the exposure levels of pulmonary delivered PRS-220, administered via oropharyngeal aspiration, to the intravenously delivered

Fig. 1 | Structural evolution and binding properties of PRS-220. a Structural models comparing NGAL (Anticalin scaffold, PDB ID: 1DFV), an intermediate, and PRS-220 highlighting the evolution of residue variations towards high affinity binding to CCN2 and favorable biophysical properties (higher Tm). Yellow sticks: disulfide bond. Red and orange spheres: residues that were mutated in Lcn2 to generate the intermediate. Blue spheres: Cα atoms of residues that remained fixed during subsequent engineering steps towards PRS-220. Graphs were generated with Pymol. **b** Binding of PRS-220 to recombinant CCN2, CCN2 N-terminal fragment (IGFBP & vWC) and C-terminal fragment (TSR & CT domain) by ELISA ($n = 3$ experiments, mean ± SD). **c** Competition of PRS-220 and the Anticalin scaffold (NGAL ctrl) with pamrevlumab for binding to CCN2 ($IC_{50} = 0.35$ (± 0.05) nM) and competition of pamrevlumab with itself for binding to CCN2 ($IC_{50} = 1.14$ (± 0.03) nM) analyzed by ECLA ($n = 3$ experiments, mean ± SD). **d** Experimental setup of the competition ECLA. Created in BioRender. Pavlidou, M. (2025) https://BioRender.com/y92y274 **e** Quantification of PRS-220 binding to CCN2 expressed by TGF-β1-activated normal human lung fibroblasts ($n = 3$ experiments, mean+SD). Dotted line represents background signal in presence or absence of 5 ng/mL TGF-β1 with anti-scaffold detection antibody only. **f** Schematic view of air-liquid interface (ALI) cell culture model for investigation of mucus interaction. Created in BioRender. Pavlidou, M. (2025) https://BioRender.com/j57y046 **g** Confocal imaging (63x) of PRS-220 mucus penetration in ALI cultures of cystic fibrosis derived human bronchial epithelial cells (HBECs) at baseline, 0.5 min (PRS-220) or 5 min (pos. ctrl) after adding Alexa Fluor 647-labeled PRS-220 or mucus binding microspheres (positive ctrl) to the apical side. Representative images of $n = 3$ independent experiments with mucus = green, air surface liquid (ASL) =magenta, PRS-220/pos. ctrl = blue. **h** PRS-220 mucus interaction by Quartz Crystal Microbalance with Dissipation (QCMD) monitoring of the frequency shift (=changes in mucus mass) and dissipation shift (=changes in mucus hydration). Mucus solution was perfused over a chip, followed by perfusion of 10 μM PRS-220, Poly-L-lysine (PLL) as positive control for mucus interaction and PBS. Source data are provided as a Source Data file.

Table 1 | Post-nebulized integrity analysis of a formulation containing PRS-220 at 45 mg/mL nebulized with an investigational eFlow® Nebulizer System

Test method	Test result	Comparability criteria	Pre-nebulization ($n = 1$)	Post-nebulization ($n = 3$)
Subvisible particulate matter (light obscuration)	Cumulative particulates per mL >2 µm	<Factor 10 difference	45	196
	Cumulative particulates per mL >5 µm		19	66
	Cumulative particulates per mL >10 µm		7	28
	Cumulative particulates per mL >25 µm		1	1
Turbidity	FTU (500–600 nm, blank subtracted)	≤ 10.0	3.7	2.9
cIEF	Main peak [%]	≥ 75.0	82.4	83.1
	Acidic peaks [%]	-	17.6	16.9
	Basic peaks [%]	-	Not detected	Not detected
SEC	Main peak [%]	≥ 95.0	99.7	99.7
	HMWS [%]	≤ 5.0	0.3	0.3
	LMWS [%]	-	Not detected	Not detected
ECLA	Relative potency [%]	80 – 120	105	100

Results from light obscuration, turbidity, isoelectric focusing (cIEF), size exclusion chromatography (SEC) and potency (ECLA) measurements are shown.

Table 2 | Aerodynamic properties of a formulation containing PRS-220 at 45 mg/mL when nebulized with an investigational eFlow® Nebulizer System

Test method	Parameter	Result
Next Generation Cascade Impactor	Mass median aerodynamic diameter	3.7 - 4.2 µm
	Geometric standard deviation	1.5 – 1.7
	Fine particle fraction <5 µm	65 – 77%
Breathing Simulator	Delivered dose in % of emitted dose	57 – 63%
	Drug delivery rate	12.1 – 15.6 mg/min

Performance parameters determined for three devices measured by next generation cascade impactor (NGI) and breathing simulator using the adult breathing pattern are shown.

monoclonal antibody pamrevlumab in bronchoalveolar lavage fluid (BALF), lung tissue and plasma when administered at the same dose level. PRS-220 achieves a high exposure in lung tissue and a low plasma exposure (Fig. 2a) with only 0.9% of the lung delivered drug reaching the circulation (Supplementary Table 2) while pamrevlumab shows a higher plasma exposure than PRS-220 with only 20% of the systemically delivered antibody reaching the lung (Fig. 2b, Supplementary Table 2). Comparing peak concentrations (C_{max}) in lung and plasma, lung delivery of PRS-220 achieves an 80-fold higher C_{max} in the lung than pamrevlumab, which reaches a much higher C_{max} in plasma, when the same absolute amount of both compounds was administered via the different administration routes (Fig. 2c). In addition to the pharmacokinetic (PK) profiles, we investigated the tissue distribution of fluorescently labeled PRS-220 and pamrevlumab in murine lung tissues by imaging, when administered as described above. We observed a strong and evenly distributed fluorescence signal for PRS-220 throughout the entire lung while systemically administered pamrevlumab was detected with very low signal intensity suggesting higher exposure levels when the drug is given via the pulmonary route of administration (Fig. 2d).

We confirmed the significant biodistribution of locally administered PRS-220 in fibrotic lungs by light sheet microscopy of the whole left lung in the bleomycin-induced lung fibrosis mouse model. Whole lung imaging showed that PRS-220 can be detected in the airways but also penetrates the more distal alveolar and interstitial regions of the fibrotic lung, which are of particular relevance for the development of lung fibrosis (Fig. 2e, f). Using a deep learning algorithm for automated identification of fibrotic areas, we determined the drug coverage specifically in the fibrotic tissue by quantifying fibrotic tissue that showed a drug signal. When compared to systemically delivered pamrevlumab, PRS-220 achieved a 12-fold higher coverage of fibrotic tissue 2 h after administration. This superior profile persisted over the whole study time course indicating a more

https://doi.org/10.1038/s41467-025-58568-x

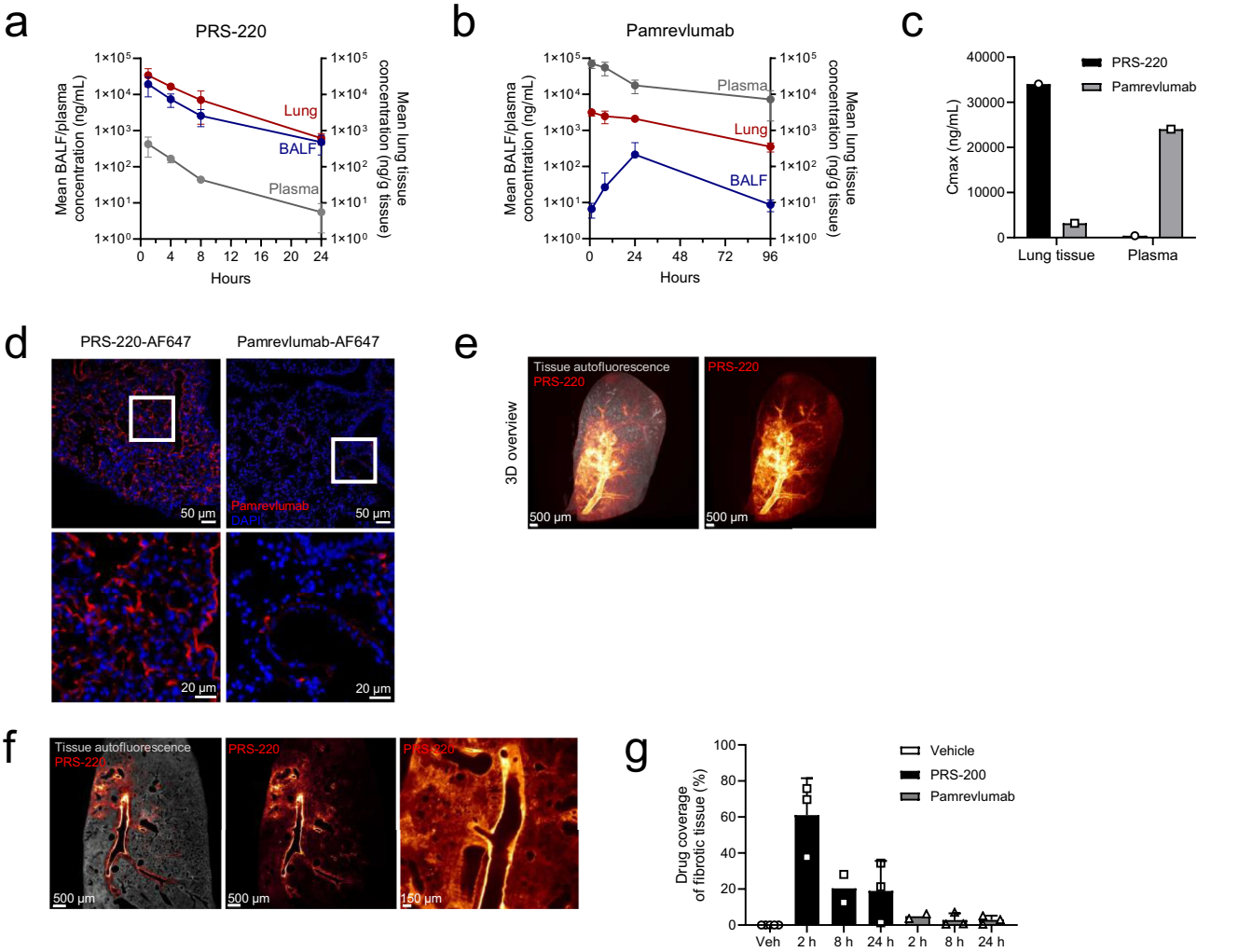

Fig. 2 | Pulmonary delivery of PRS-220 achieves superior lung tissue penetration when compared to systemic delivery of an antibody. a PK of PRS-220 in BALF, lung tissue, and plasma at 1 h, 4 h, 8 h and 24 h after delivery to the lungs of healthy mice by oropharyngeal aspiration (100 µg/mouse, $n = 4$ animals per timepoint, mean ± SD). **b** PK of pamrevlumab in BALF, lung tissue, and plasma 1 h, 8 h, 24 h and 96 h after intravenous delivery to healthy mice (100 µg/mouse, $n = 4$ animals per timepoint, mean ± SD). **c** Comparison of lung tissue and plasma peak concentrations (C_{max}) of PRS-220 and pamrevlumab determined by non-compartmental analysis of PK data shown in (**a**, **b**). **d** Alexa Fluor 647-labeled PRS-220 (PRS-220-AF647) and pamrevlumab (pamrevlumab-AF647) imaged in lung tissue sections 2 h after administration to healthy mice. PRS-220-AF647 was delivered to the lung by oropharyngeal aspiration and pamrevlumab-AF647 was administered intravenously (both at 100 µg/mouse). Figure shows representative images of $n = 4$ animals per treatment group for PRS-220 and pamrevlumab (both in red) and cell nuclei (DAPI, blue) at 4x and 80x magnification. **e** Alexa Fluor 647-labeled PRS-220 (100 µg/mouse) delivered to fibrotic lungs of mice at day 21 after bleomycin challenge by oropharyngeal aspiration imaged by light sheet microscopy. Figure shows representative whole left lung imaging of PRS-220 2 h after dosing (scale bars 500 µm). Experiment was performed with $n = 5$ animals (vehicle) and $n = 3$ animals (all other treatment groups). **f** Magnified 2D sections generated from 3D scanned lung (scale bars 500 µm & 150 µm) shown in (**e**). **g** Compound accumulation of PRS-220 delivered to the lung and pamrevlumab administered intravenously (both 100 µg/mouse) in fibrotic lung tissue determined by light sheet imaging & quantitative analysis. Data is shown as mean ± SD including single data points of individual mouse lungs ($n = 5$ (vehicle)); $n = 3$ (PRS-220 2 & 24 h, pamrevlumab 8 & 24 h); $n = 2$ (PRS-220 8 h, pamrevlumab 2 h). Source data are provided as a Source Data file.

efficient targeting of the fibrotic lesions by pulmonary drug delivery (Fig. 2g).

Feasibility and PK profile assessment of inhaled delivery in vivo

For the initial in vivo characterization presented so far, PRS-220 was delivered as a bolus to the lungs of mice, which is the most commonly used approach for pulmonary drug delivery in vivo. In a next step, we established a protocol to deliver aerosolized PRS-220 to rodents via nose-only inhalation. Although this is technically more challenging, it translates better to the delivery in humans. At the same time, nose-only inhalation is less invasive, better tolerable and does not require anesthesia allowing for longer efficacy studies that reflect the chronic phenotype of the disease. We analyzed the PK profile of nebulized PRS-220 administered by inhalation. PRS-220 was applied to healthy rats via nose-only inhalation at mean achieved delivered dose levels of 5.6, 18.1 and 57 mg/kg daily for 4 consecutive days (Fig. 3a). After inhaled administration, maximal serum concentrations were reached after 2.5–3 h, and declined thereafter with half-life ($t_{1/2}$) values ranging from 2.2 to 4.5 h on Day 1, and 4.3 to 6.6 h on Day 4. High, dose-dependent exposure in lung tissue over 24 h with a lung/serum C_{max} ratio of ~300 was observed for all three dose levels, while systemic bioavailability was very low (2.2–3.7%) with dose-normalized $AUC_{0\text{-}22h}$ values of 120–200 h*ng/mL after inhaled delivery and 5500 h*ng/mL after intravenous administration (Fig. 3b, Supplementary Table 3). In contrast to inhaled delivery, systemic administration of PRS-220 by intravenous injection resulted in a rapid decline of exposure and fast

https://doi.org/10.1038/s41467-025-58568-x

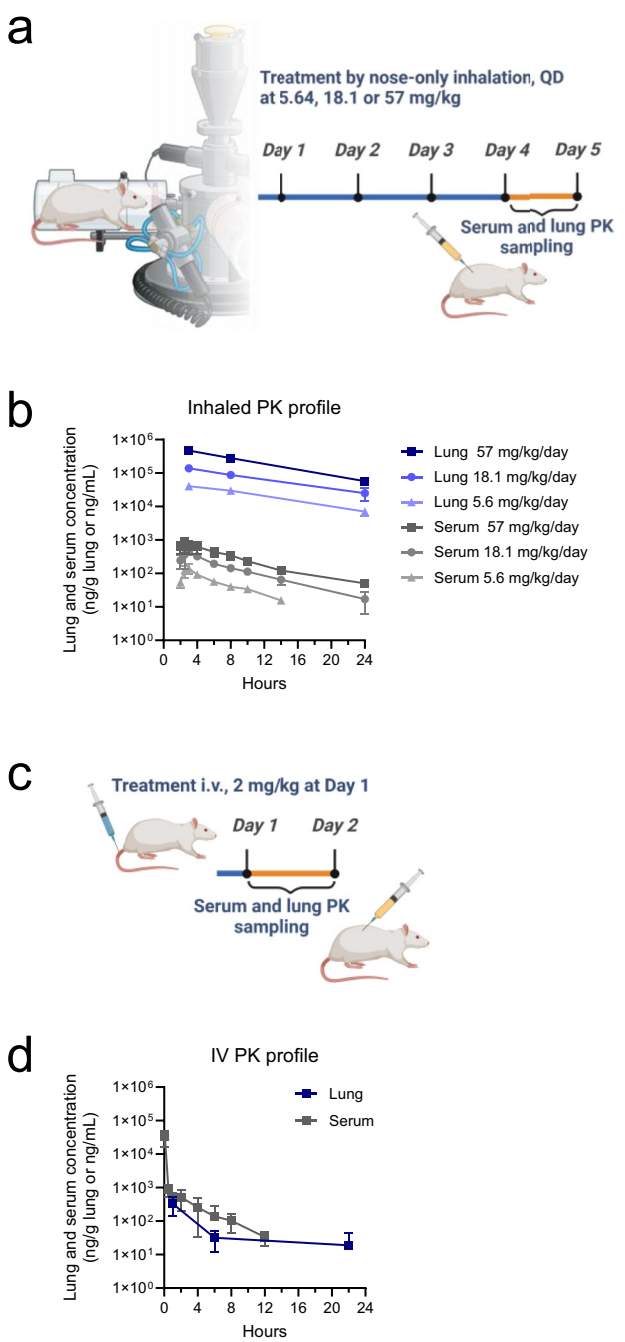

Fig. 3 | Inhaled delivery of PRS-220 achieves high, dose-dependent lung exposure with low systemic bioavailability in vivo. a Scheme outlining the design of a study to investigate the PK profile of daily (QD) inhaled PRS-220 in lung tissue and serum of healthy rats. Rats were treated daily with PRS-220 at 3 different dose levels by nose-only inhalation for 4 days. Created in BioRender. Pavlidou, M. (2025) https://BioRender.com/e13e683 **b** Serum and lung exposure of free, non-target bound PRS-220 was determined over time after daily treatment with 3 different dose levels by nose-only inhalation for 4 days. Graph shows PRS-220 levels above the detection limit as mean ± SD of $n = 6$ animals (3 male and 3 female) per timepoint in serum and lung tissue. Figure legend indicates the mean achieved delivered dose levels during the study. **c** Scheme outlining the design of a study to investigate the PK profile of a single intravenous (i.v.) administration of PRS-220 in lung tissue and serum of healthy rats. Created in BioRender. Pavlidou, M. (2025) https://BioRender.com/z18p244 **d** PRS-220 levels upon single intravenous administration at a dose level of 2 mg/kg were assessed in lung tissue and serum. Graph shows PRS-220 levels above the detection limit as mean ± SD of $n = 6$ animals (3 male and 3 female) per timepoint in serum and lung tissue. Source data are provided as a Source Data file.

elimination in serum ($t_{1/2} = 2.2$ h) as expected based on the low molecular weight of the protein and very low exposure in the lung tissue (lung/serum C_{max}: 0.03) (Fig. 3c, d). In conclusion, we confirmed the feasibility of administering nebulized PRS-220 to rodents via an inhalation tower resulting in dose-dependent exposure of the drug in the lung tissue. Despite the technical challenges, inhaled delivery to study nebulized drugs in animals is physiologically more relevant than the oropharyngeal route of administration and is therefore the more appropriate approach for lung delivery in in vivo studies. For the following in vivo studies, nebulized PRS-220 was delivered to rodents by inhalation to better mimic the delivery in humans.

Deep penetration of fibrotic lung tissue by inhaled PRS-220 translates into pronounced attenuation of fibrosis in vivo

In the following experiments, we aimed to characterize the lung biodistribution and anti-fibrotic activity of inhaled PRS-220 in the silica-induced lung fibrosis mouse model, a physiologically highly relevant disease model to study lung fibrosis[39]. We monitored the progressive phenotype of this model and observed that on day 41 post silica challenge a pronounced fibrotic lung remodeling had occurred as demonstrated by the much denser tissue structure of silica challenged lungs (Fig. 4a). Next, we investigated the impact of fibrotic lung remodeling and impairment of the lung architecture on drug exposure in silica-treated mice by assessing the PK profile of inhaled PRS-220 in comparison to healthy, untreated mice. The PK analysis revealed similar, dose-dependent exposure profiles of PRS-220 in lung tissue and plasma of healthy and silica challenged mice suggesting that fibrotic remodeling of the lung does not significantly alter the PK behavior of the inhaled drug (Fig. 4b). In both, healthy and silica challenged mice, we observed a high exposure of PRS-220 in the lung at the site of the expected target engagement whereas only ~1–5% of the drug was present in the circulation. Additionally, lung imaging confirmed very efficient penetration and drug distribution in the pharmacologically relevant areas of the fibrotic lung (Fig. 4c and Supplementary Fig. 2a). In a comprehensive imaging-based analysis, PRS-220 was not only identified in the lining of the airway epithelium but also penetrated more distal regions of the lung including alveolar and interstitial lung tissues (Fig. 4d, e). Importantly, we detected PRS-220 in proximity and adjacent to CCN2 expressing cells, including bronchial and alveolar epithelial cells, supporting efficient delivery of PRS-220 to its target in the fibrotic lung via inhalation (Fig. 4f).

Having confirmed the efficient tissue penetration of inhaled PRS-220 and its delivery in proximity to its target, the anti-fibrotic activity of PRS-220 administered by daily (QD) inhalation in comparison to intravenous delivery of pamrevlumab given every second day was tested in the previously established 42-day silica model (Fig. 4g). The dose level of pamrevlumab (10 mg/kg every other day (Q2D)) was chosen based on published data and on our PK study showing pronounced drug exposure when applying this dose regimen[27].

Total collagen deposition in the lung as an indicator of fibrotic tissue remodeling was measured by quantification of total lung hydroxyproline, which was significantly upregulated by the silica challenge as shown for the vehicle control groups (Fig. 4h). Daily inhaled administration of PRS-220 led to a significant reduction of total collagen deposition in the lung in comparison to inhaled delivery of the vehicle control (Fig. 4h). Of note, the decrease in total lung collagen by PRS-220 was more pronounced when compared to effects of systemic treatment with pamrevlumab. We also detected a significant reduction of lung weights by PRS-220 treatment in silica challenged mice confirming that the treatment attenuated lung damage (Supplementary Fig. 2b). Moreover, Ccl2 and Timp1 mRNA expression, markers of lung injury and fibrotic tissue remodeling and significantly induced upon silica challenge, were found downregulated in lung tissue of PRS-220 treated mice (Fig. 4i, j). Overall, studies in the silica model confirmed effective delivery of PRS-220 to fibrotic lungs of mice translating into more

https://doi.org/10.1038/s41467-025-58568-x

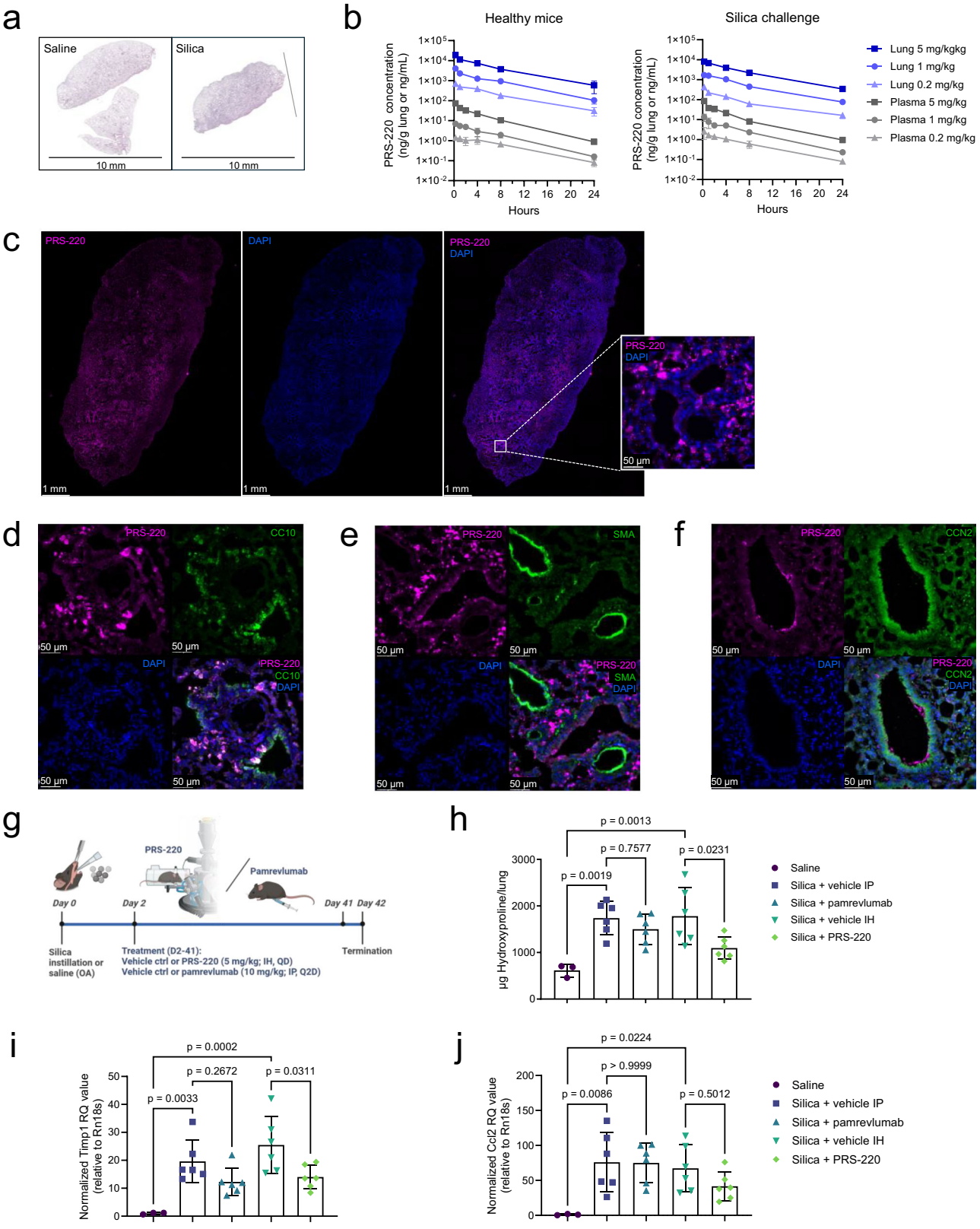

pronounced anti-fibrotic activity when compared to a systemically delivered monoclonal antibody against the same target.

Establishment of an ex vivo lung perfusion model to study deposition of nebulized PRS-220 in the human lung

After in depth characterization in mouse models and towards a comprehensive characterization of inhaled drug delivery in humans, we aimed to investigate the drug delivery profile of PRS-220 in human ex vivo models to better predict the drug performance for its later inhaled application in humans. To circumvent the considerable challenges of investigating drug deposition in the human lung due to the lack of suitable models, we established an ex vivo lung perfusion (EVLP) model to investigate pulmonary drug deposition following inhaled delivery in whole human donor lungs (Fig. 5a, b). We set up the

Fig. 4 | Deep penetration of fibrotic lung tissue by PRS-220 upon inhalation translates into superior attenuation of fibrosis in vivo. a Fibrotic remodeling of the lung assessed 41 days after silica challenge in comparison to saline challenge of mouse lungs by Hematoxylin and Eosin staining. **b** PK profile of PRS-220 in lung tissue and plasma delivered via nose-only inhalation at 3 dose levels (0.2, 1 and 5 mg/kg targeted delivered dose) to healthy or silica challenged mice. Graph shows data of $n = 4$ animals per group and timepoint as mean ± SD. **c** Immunofluorescence imaging of PRS-220 (magenta) 2 h after inhaled delivery to fibrotic, silica-challenged mouse lungs (day 41, targeted delivered dose 5 mg/kg). Cell nuclei are stained with DAPI (blue). **d** Co-immunofluorescence staining of PRS-220 (magenta), club cell marker CC10 (green) and **e** smooth muscle cell & myofibroblast marker aSMA (green) in lung tissues from **c**. **f** Localization of PRS-220 (magenta) in relation to cells expressing its target assessed by co-immunofluorescence imaging of PRS-220 and CCN2 (green) in lung tissues from **c**. **g** Scheme of the in vivo efficacy study in mice. Created in BioRender. Pavlidou, M. (2025) https://BioRender.com/x52k357 **h** Total collagen deposition in the lung by measuring lung hydroxyproline. Individual data points of $n = 3$ (saline) and $n = 6$ (all other) animals per treatment group including mean ± SD are shown (One-way ANOVA with Šídák's multiple comparisons test; $^{*}p \le 0.05$, $^{**}p \le 0.01$, ns (not statically significant) $p > 0.05$). **i** Lung tissue mRNA gene expression of Timp1 and **j** Ccl2 with Rn18s serving as reference gene. Individual data points of $n = 3$ (saline) and $n = 6$ (all other) animals per treatment group including mean ± SD are shown (One-way ANOVA with Šídák's multiple comparisons test; $^{*}p \le 0.05$, $^{**}p \le 0.01$, $^{***}p \le 0.001$, ns (not statically significant) $p > 0.05$). For all imaging analyses, representative images of in total $n = 4$ mice per treatment group are shown. Source data are provided as a Source Data file.

EVLP system placing the nebulizer in-line with the ventilation system/tubing to assure efficient delivery of the nebulized, fluorescently labeled PRS-220 to the ex vivo ventilated and perfused human lungs (Supplementary Fig. 3a). PRS-220 was delivered at a dose of 6.4 mg per lung. Pulmonary deposition of nebulized PRS-220 for up to 4 h after administration was analyzed in lung biopsies by imaging. We observed broad, pronounced deposition of PRS-220 in different areas of the human lung 4 h after inhaled drug delivery (Fig. 5c). Co-immunofluorescence imaging of different cell markers, including α smooth muscle actin (αSMA) for smooth muscle cells surrounding airways and vasculature, platelet-derived growth factor receptor α (PDGFRα) for both smooth muscle cells and lung fibroblasts, and keratin-5 (KRT5) for epithelial cells, were applied to investigate drug distribution on a more detailed, cellular level 2 h and 4 h after PRS-220 delivery (Fig. 5d–f, Supplementary Fig. 3b–d). We detected PRS-220 in the airways lining the airway epithelial surface and in the more distal regions of the lung including the alveoli and lung interstitium at both timepoints, providing evidence of the compound's ability to effectively penetrate the lung tissue. Importantly, we found PRS-220 localized in proximity to CCN2 expressing cells, supporting its strong potential for efficient target engagement across the human lung.

In silico inhalation study shows a broad distribution of aerosol deposition in healthy and IPF lungs

To further investigate the drug deposition upon inhalation in healthy and diseased lungs, we performed in silico inhalation studies on lungs from one healthy subject and two IPF patients of mild and severe disease (Supplementary Table 4 and 5). For this purpose, subject- and disease-specific, high-fidelity simulation models were created, mainly based on information from high-resolution chest CT images (Fig. 6a) resulting in a 3D model geometry including the entire airway tree and alveolar tissue (Fig. 6b). Computer simulations of the airflow, local tissue deformation, and particle dynamics over a full inhalation and exhalation cycle with device-specific aerosol characteristics were performed to predict aerosol deposition (Fig. 6c). These visual representations demonstrate that the aerosol is broadly distributed throughout all regions of the lung in each of the three cases. This is an important finding for the heterogeneously diseased lungs, confirming the feasibility of targeting both already fibrotically distorted tissue predominantly located in paraseptal or subpleural areas of the lung and the surrounding, not yet fibrotically remodeled lung tissue, to prevent disease progression at the same time.

Leveraging the single-particle resolution of the approach and the completeness of the model domain, detailed statistics about the spatial distribution of deposited aerosol in the entire respiratory system can be obtained. The mass fraction of deposited aerosol (%) was analyzed per category (Fig. 6d). The results are similar for all cases with about 55% being deposited in the targeted alveolar tissue, about 30% deposited in the conducting airways, 9% deposited in the mouth/throat region and <9% of exhalation losses. The main reason for this high overall efficiency is hypothesized to be related to the favorable particle size distribution. The similar overall efficiency in all cases is probably a result of using the same aerosol (see methods for details) and same breathing pattern (sinusoidal flow, 500 mL tidal volume, 15 breaths/min, 1:1 insp./exp. ratio). This seems to outweigh the variability caused by subject-specific lung geometry or disease state. The differences between healthy and diseased lungs, however, become clearly visible when looking at the aerosol mass concentration in healthy versus fibrotic regions of the lung (Fig. 6e). For clarity, mass concentrations have been normalized with the volumes of the healthy and fibrotic region, respectively. As a consequence, values smaller/greater than 100% indicate under/over-proportional deposition in the respective sub-volume. For the severe IPF case, the aerosol concentration is considerably smaller in fibrotic regions, which is expected due to higher tissue stiffness and therefore less ventilation of these regions. The same effect, although smaller, can be observed for the mild disease state. Overall, this novel in silico approach shows that the inhaled drug can still be deposited in areas of massive disruption of the lung architecture which strongly supports the concept of local drug delivery for treatment of IPF.

PRS-220 reduces fibrotic remodeling in a human model of lung fibrosis

In a final approach we aimed to further characterize the anti-fibrotic activity of PRS-220 in human IPF tissue to better predict efficacy of local CCN2 inhibition in humans. In line with recent studies analyzing CCN2 expression in IPF lungs, we identified a pronounced target expression in different regions of the lung including the proximal bronchial epithelium as well as the distal alveolar type 2 cells and interstitial regions[18,23] (Fig. 7a). These regions of the lung are all very well accessible by PRS-220 upon inhalation as demonstrated in our lung biodistribution studies. To further investigate the concept of local CCN2 targeting in the lung for optimal anti-fibrotic activity, we investigated the effect of CCN2 inhibition in IPF tissue derived human precision cut lung slices (PCLS). IPF PCLS were either treated with PRS-220, pamrevlumab, current IPF standard of care treatment nintedanib or a vehicle control for 96 h (Fig. 7b, c). Collagen1A1 (COL1A1) protein regulation was analyzed as a measure of active fibrotic remodeling in the lung tissues. Western blot analysis of COL1A1 in PCLS homogenates revealed a strong and significant downregulation of COL1A1 by PRS-220 at both concentrations tested, 100 nM and 500 nM, whereas equimolar treatment with pamrevlumab (100 nM) or treatment with high concentrations of nintedanib led to a slight but not statistically significant reduction of COL1A1 expression (Fig. 7d, e). Using this human PCLS model, which we consider as being highly translatable to the human disease, we confirmed that CCN2 blockade by PRS-220 reduces fibrotic remodeling in human IPF lung tissue. In line with the results from our in vivo study, PRS-220 blocks collagen production more potently when compared to pamrevlumab, while treatment with the current IPF

https://doi.org/10.1038/s41467-025-58568-x

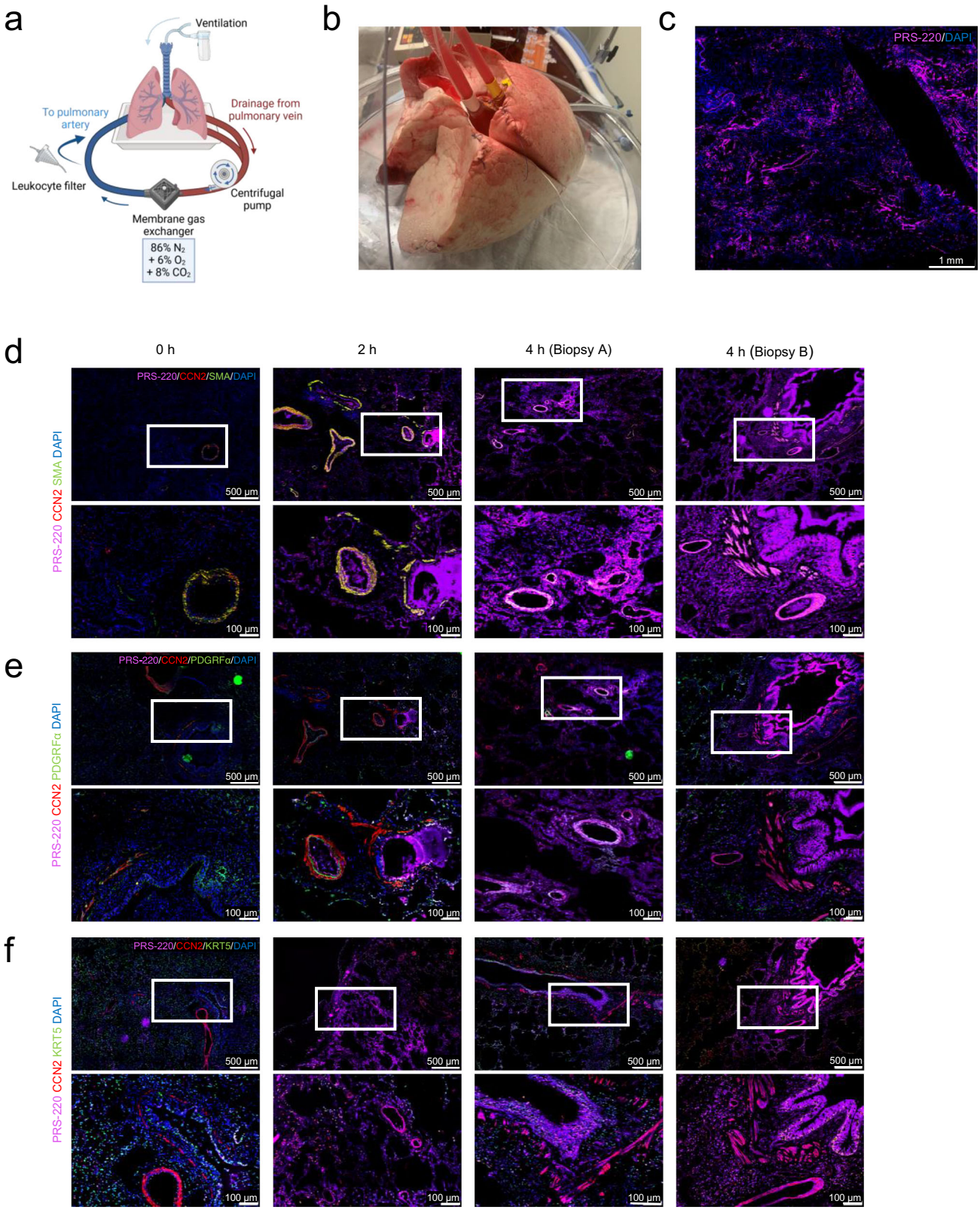

standard of care nintedanib also only conferred modest and less pronounced anti-fibrotic activity.

Discussion

Our study highlights the potential of inhaled drug delivery for treatment of chronic respiratory disease and provides a holistic approach to preclinically evaluate drug candidates for pulmonary delivery applying novel, translatable models. In this regard, we apply CCN2 targeting as a case study to highlight the potential of inhaled drug delivery in comparison to a systemically delivered monoclonal antibody.

We described the preclinical profile of PRS-220, a biotherapeutic targeting CCN2, administered directly to the lung by inhalation for treatment of pulmonary fibrosis. We show that

https://doi.org/10.1038/s41467-025-58568-x

Fig. 5 | Lung tissue distribution of nebulized PRS-220 in ex vivo ventilated and perfused human lungs. a Scheme of the ex vivo lung perfusion (EVLP) set-up with the nebulizer set-up in line with the ventilation tubing. Created in BioRender. Pavlidou, M. (2025) https://BioRender.com/f59h729 **b** Picture of the actual EVLP experiment. **c** Overview immunofluorescence imaging of EVLP lung biopsies 4 h after nebulized delivery of Alexa Fluor 647-labeld PRS-220 (magenta). Cell nuclei (stained with DAPI (blue) and scale bar 1 mm). **d** Co-staining of lung tissue sections for CCN2 (red), smooth muscle actin (SMA, green) and DAPI (blue) at baseline (0 h, serving as negative control) and 2 and 4 h after nebulized delivery of Alexa Fluor 647-labeld PRS-220 (magenta). Biopsies from two different regions of the lung were analyzed at the terminal 4 h timepoint (Biopsy A and B). Figure shows images at 2 different magnifications (scale bars 500 μm for upper images and 100 μm for images below). **e** Co-immunofluorescence imaging of PRS-220 (magenta), CCN2 (red), platelet-derived growth factor α (PDGFRα, green) and DAPI (blue). **f** Co-immunofluorescence imaging of PRS-220 (magenta), CCN2 (red), keratin-5 (KRT5, green) and DAPI (blue). Figure shows representative images from independent experiments performed with $n = 3$ human donor lungs.

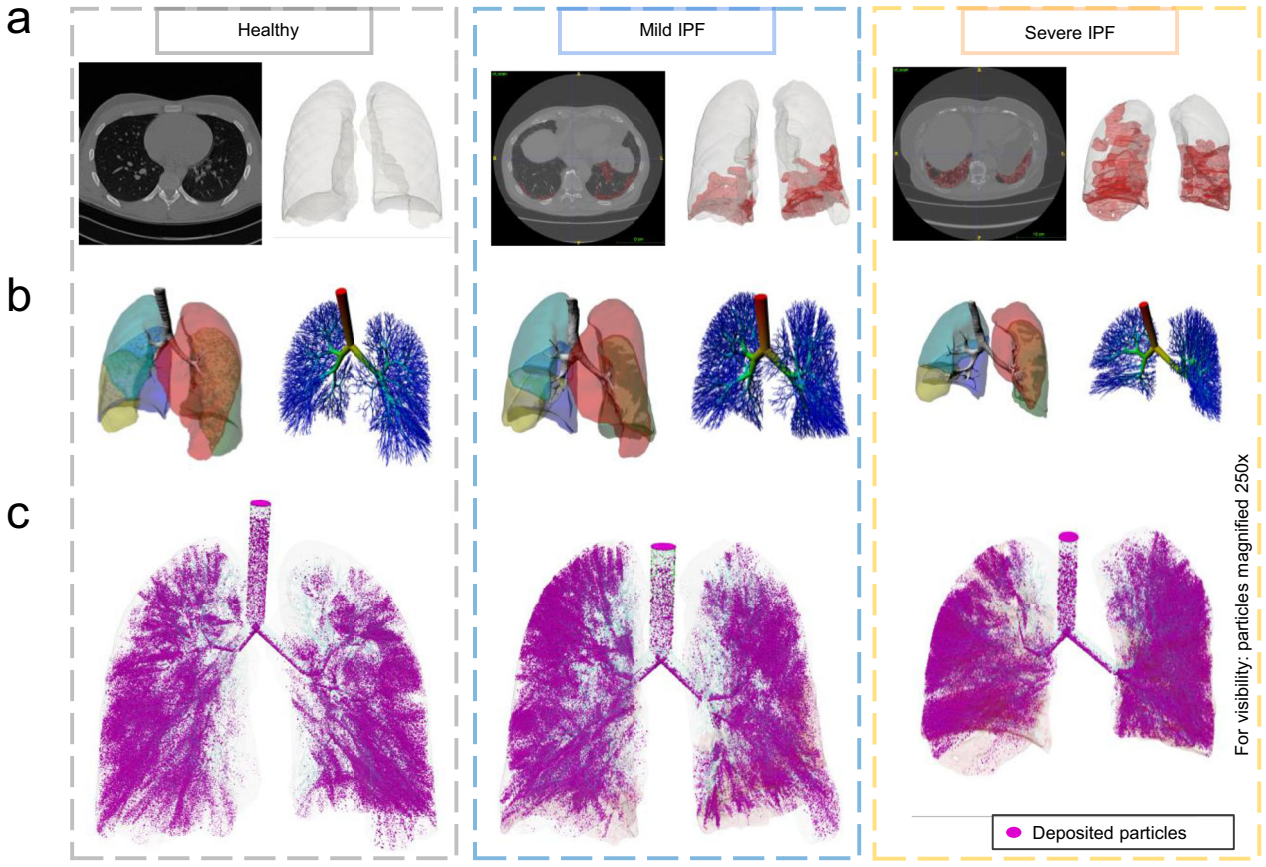

Fig. 6 | In silico inhalation study of PRS-220 in 3 human subjects shows a broad deposition pattern of PRS-220 containing aerosol in healthy and IPF lungs. a CT image analysis and segmentation of fibrotic tissue (red) and **b** airways, lungs, and lobes (left) as first step of the subject-specific model generation process. Generation of the full 16-generation tree of conducting airways (right) and visco-elastic alveolar clusters (Supplementary Fig. 4) based on segmented volumetric information and a physiology-based, space-filling growth algorithm. **c** Final pattern of deposited PRS-220 aerosol particles after simulation of airflow, particle transport and deposition for one complete breathing cycle. **d** Mass fraction of deposited aerosol per category: Mouth/throat (green), conducting airways (orange), alveolar tissue (blue), and exhaled (brown). **e** Normalized concentration of deposited aerosol mass per volume for healthy vs. fibrotic regions of the lungs (mild case = orange; severe case = red). Values smaller/>100% indicate under/over-proportional deposition in the respective sub-volume.

https://doi.org/10.1038/s41467-025-58568-x

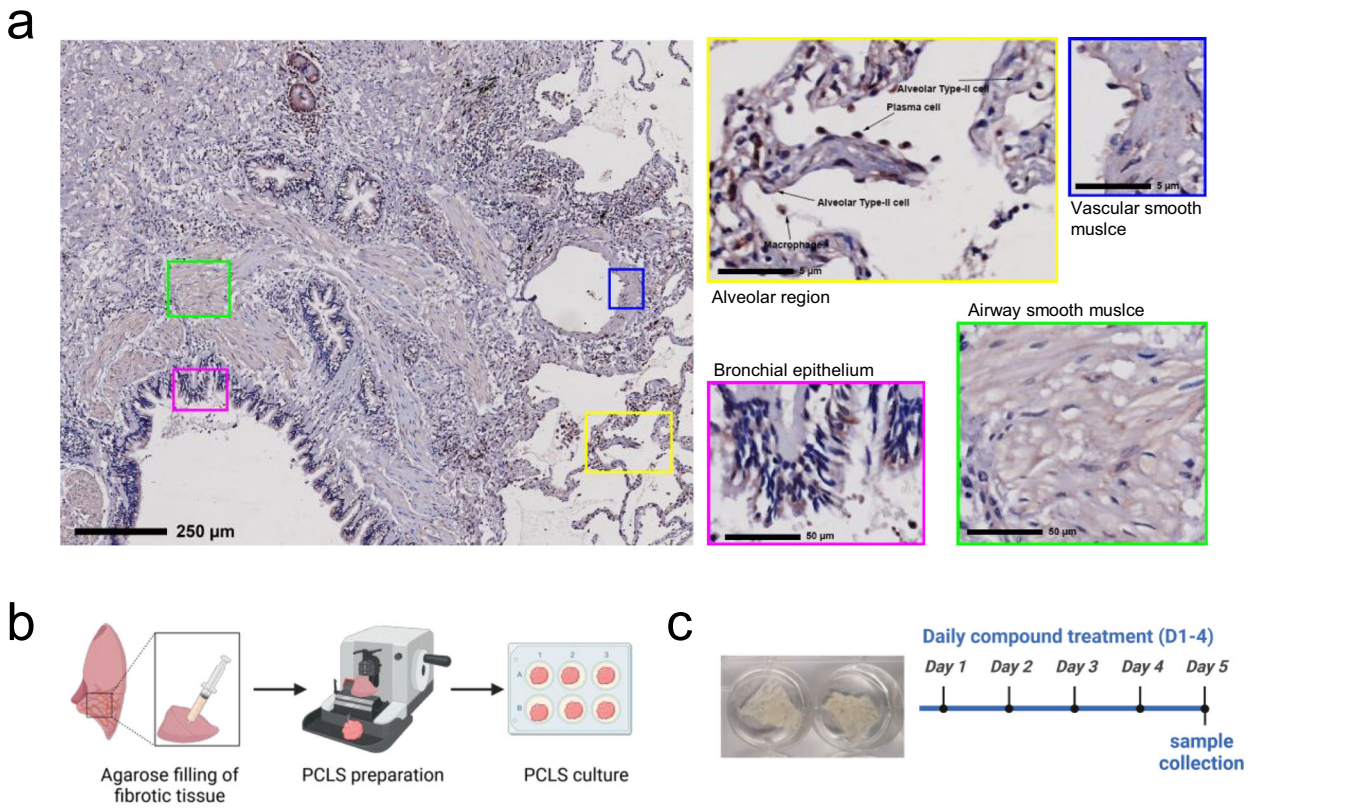

Fig. 7 | CCN2 inhibition by PRS-220 attenuates fibrotic remodeling in a human precision cut lung slice (PCLS) model of IPF. a Histopathological analysis of CCN2 expression in IPF lung tissue. Representative images of lung tissue sections from $n = 16$ different IPF patients are shown. **b** Experimental procedure of PCLS model. Created in BioRender. Pavlidou, M. (2025) https://BioRender.com/b00o965 **c** Experimental design of an ex vivo proof of concept study to investigate the anti-fibrotic effect of CCN2 inhibition by PRS-220 in PCLS from IPF patients. PCLS were treated daily with PRS-220 (100 nM and 500 nM), pamrevlumab (100 nM) and nintedanib (2 µM). Treatment with PRS-220 vehicle served as a control. PCLS were harvested at day 5 for analysis of Collagen1A1 protein levels. Created in BioRender. Pavlidou, M. (2025) https://BioRender.com/y24t356 **d** Collagen1A1 (COL1A1) protein analysis by Western blot with GAPDH serving as a loading control. Figure shows representative immunoblots of experiments performed with lung tissue from $n = 3$ IPF patients with $n = 4$-5 technical replicates per IPF donor. Arrows indicate COL1A1 protein bands subjected to densitometric analysis. **e** Densitometric analysis of COL1A1 signal in Western blots. Single data points show integrated density values (IDV) of COL1A1 signal normalized to loading control GAPDH of all technical replicates from PCLS of in total $n = 3$ IPF lung tissue donors ($n = 4$ technical replicates per treatment group for donor 1 & 2 and $n = 5$ per treatment group for donor 3; Kruskal-Wallis test with Dunn's multiple comparison; $^{***}p < 0.001$, ns (not statistically significant) $p > 0.05$). Source data are provided as a Source Data file.

PRS-220 binds to its target with high affinity and specificity. Based on its overall favorable biophysical properties it is well suited for inhaled delivery, which has been confirmed by a comprehensive assessment of lung biodistribution and PK in rodents in vivo and by applying novel, human-based ex vivo and in silico models in both normal and fibrotic lungs. Importantly, we also showed that the profile translates into superior anti-fibrotic activity when tested in state-of-the-art disease models in vivo in mice or ex vivo using human PCLS. In our work, we used a variety of approaches to investigate this CCN2 antagonist showing suitability for inhaled administration that directly translates into a superior pharmacological efficacy over systemic administration.

Inhaled drugs have been successfully applied for the treatment of respiratory diseases for decades and show potential for lung conditions that are still difficult to treat, such as IPF[40,41]. Oral inhalation allows for drug delivery directly to the lung rapidly achieving high drug levels at the site of the disease with overall low systemic exposure[1]. Until now, however, only a few drug candidates, mainly small molecules bearing the risk of unspecific targeting, have been developed for pulmonary delivery for treatment in IPF[2,42]. Inhaled

biopharmaceuticals are of particular interest as they can be designed towards high affinity and specificity reducing potential off-target toxicity. However, proteins tend to destabilize during aerosolization due to large air-liquid interfaces as well as shear and heat stresses generated during the process[5,43]. These can cause unfolding, aggregation, deamidation and other modifications of the protein leading to unknown safety consequences and to a potential loss of potency. Larger proteins such as monoclonal antibodies, widely used for systemic delivery, are known to be particularly vulnerable to such changes[44,45]. Thus, the number of biotherapeutics suited for pulmonary delivery is limited. In contrast to monoclonal antibodies, Anticalin proteins are better suited for aerosolization due to their smaller size of ~20 kDa (1/8 of an antibody) and compact, beta-barrel structure[8,12]. The present study shows that the structural integrity of the Anticalin protein PRS-220, unlike monoclonal antibodies, is maintained upon nebulization when using a vibrating mesh nebulizer.

For an inhaled intervention, it is critical to confirm efficient drug coverage of the target regions in the lung. The measured particle size distribution of aerosolized PRS-220 is sufficiently broad to cover different areas of the lung as intended given that CCN2 is broadly expressed in the lung, including both fibrotic and adjacent tissues of still normal lung architecture which need to be protected from further disease progression. We showed preclinically that delivering PRS-220 directly into the lung leads to higher lung exposure and advanced tissue biodistribution in both fibrotic and healthy lung tissue compared to the systemically administered pamrevlumab. This is in line with literature reporting that only ~15% of systemically administered monoclonal antibodies reach the lung[46–49]. For small molecule drugs, inhalation has also been reported to achieve superior exposure in the lung when compared to systemic delivery[50]. The investigation of lung biodistribution of inhaled drugs in human lungs remains challenging because of the lack of preclinical models and the requirement of costly and time-consuming clinical imaging studies using labeled drugs which only provide data of limited spatial resolution[51,52]. We aimed to overcome these limitations by establishing an ex vivo lung perfusion model of whole human donor lungs which enabled us to confirm broad tissue deposition of PRS-220 in proximity to its target CCN2 at a high, cellular resolution in the lung tissue over time. Up to now, EVLP models were only applied to determine absolute drug levels in BALF or perfusate for studying pulmonary drug absorption of inhaled small molecules or penetration of systemically delivered drugs, while in-depth lung imaging studies assessing drug distribution on microscopic level have not been performed[53–56]. This EVLP model can be further developed for analysis of drug distribution in diseased human lung tissues, for example when using lung tissues of IPF patients. To investigate whether fibrotic remodeling impacts inhaled drug delivery, we developed a physics/artificial intelligence-based in silico model simulating inhaled drug deposition in lungs of actual IPF patients, building upon a previously generated and validated model of healthy subjects (manuscript under review)[57]. Here, we confirmed that inhaled PRS-220 achieves a broad deposition in healthy and fibrotic tissue including peripheral areas of lung, which is in line with results of two imaging studies of inhaled small molecule drugs performed in IPF patients[58,59].

Although the two approved drugs for IPF treatment, nintedanib and pirfenidone, have been shown to reduce lung function decline and mortality of patients, IPF still remains a devastating and ultimately fatal disease with a high medical need for novel therapies[14]. Despite many attempts to develop new effective and well tolerated therapies, failure rates during clinical development remain very high[60]. Drug development has been challenged by the lack of translatability of preclinical models and non-predictivity of preclinical data for clinical efficacy. Very often animal models do not capture important characteristics of human disease, such as the progressive nature of the disease and its histopathology[60,61]. Thus, robust and translatable preclinical data packages, preferentially including human model systems such as PCLS, are required to de-risk clinical development[62,63]. In our study, we applied a human IPF PCLS model to demonstrate superior potency of PRS-220 in blocking COL1A1 expression when compared to the CCN2 antibody pamrevlumab and the small molecule drug nintedanib. The difference in potency compared to pamrevlumab is likely driven by the higher affinity of PRS-220 to its target while its smaller size could also allow for better targeting of CCN2 in the dense fibrotic tissue. To the best of our knowledge, until now no data has been published describing the anti-fibrotic effect of CCN2 inhibition in this model. IPF standard of care treatment nintedanib has been reported to decrease fibrotic remodeling and collagen turnover in IPF PCLS in other studies suggesting that this preclinical data may indeed be predictive for later effects in IPF patients[64,65]. At the same time, our study shows that CCN2 inhibition by PRS-220 may be more potent than nintedanib treatment although potential synergistic effects of both treatments require further investigation.

Another important aspect of our work is the development of better translatable in vivo models and drug delivery techniques. Based on its progressive phenotype and similarities in histopathology, the silica-induced mouse model is considered highly translatable to a fibrotic lung disease in humans called 'silicosis', triggered by inhalation of occupational dusts and particles[39]. Of note, its relevance is emphasized by the fact that the approved IPF treatment nintedanib was also effective in this model[66,67]. While most of these studies apply shorter models of 4 weeks duration, we developed a prolonged, 6 weeks silica-induced lung fibrosis model to study the therapeutic potential of PRS-220 during the fibrotic phase. Moreover, we delivered PRS-220 by nose-inhalation of aerosolized PRS-220 to better mimic the drug delivery in humans and to reduce the burden and invasiveness of drug delivery for animals because - unlike other pulmonary delivery techniques - nose-only inhalation does not require anesthesia of animals. Applying the prolonged silica model and inhaled drug delivery, we also confirmed superior efficacy of PRS-220 over pamrevlumab in the silica-induced lung fibrosis mouse model. Additional prolonged models reflective of the fibrotic phenotype could be addressed for inhalation efficacy studies by further research. While the repetitive bleomycin mouse model would qualify as such model, technical challenges need to be overcome such as bleomycin-induced toxicity (e.g. body weight loss) in combination with the stress put upon animals by repeated inhaled drug delivery.

In a phase 2 clinical trial, CCN2 blockade was shown to reduce the lung function decline in patients with IPF on treatment with the systemically administered monoclonal antibody pamrevlumab[31]. However, these findings were not confirmed in a subsequent phase 3 clinical trial leading to the discontinuation of the program in IPF[32]. It is unclear why the drug failed to meet the clinical endpoints. The role of CCN2 as a key mediator of fibrosis in various organs is highly recognized and its role in fibrosis has been confirmed on a genetic level[16,22]. As demonstrated by us and other studies, CCN2 is highly upregulated in different compartments of the fibrotic lung including fibroblasts[22]. Moreover, the role of CCN2 has been evaluated in a plethora of preclinical studies involving different in vivo models of lung fibrosis and approaches to inhibit CCN2, including genetic studies showing that specific deletion of CCN2 in lung cells blocks fibrotic lung remodeling in different models of pulmonary fibrosis in mice thereby highlighting the potential of local CCN2 targeting in the lung[24,27,28,30]. Direct, preclinical comparison of inhaled PRS-220 with the antibody pamrevlumab regarding lung exposure and efficacy shows an overall better profile of PRS-220, suggesting that higher target affinity and local target engagement might translate into more meaningful outcomes in patients. Pamrevlumab also did not meet its primary endpoint in a phase 2 clinical study of diabetic nephropathy where a lack of tissue penetration has been discussed as potential reason for its failure[16].

Several other systemically delivered monoclonal antibody failed to demonstrate anti-fibrotic activity in IPF clinical trials, including for example the anti-LOXL-2 antibody simtuzumab not meeting its primary endpoint in a phase 2 clinical study despite promising preclinical data[68]. It requires further investigation to determine whether the failure of these programs for IPF treatment is – at least partly – related to a generally limited lung tissue penetration and exposure of systemically delivered monoclonal antibodies.

In conclusion, our study highlights the potential of inhaled drug delivery for treatment of lung fibrosis while emphasizing the importance of applying translatable preclinical models and physiologically relevant methods of drug delivery.

Methods

Ethics statement

All experiments involving human lung tissues were performed in accordance with the Declaration ofHelsinki and written informed consent was obtained from all participants. Ethical approval of the studies is highlighted in the respective method sections.

All animal experiments were conducted according to guidelines and laws of the respective organizations conducting the different studies, including Animal Health Regulation 2010/63/EU for all studies conducted within the European Union and national guidelines:

Mouse PK studies and lung biodistribution studies in bleomycin treated mice carried out at Fidelta were in accordance with Croatian national legislation (Official Gazette 55/13) and approved by the Ministry of Agriculture, Veterinary and Food Safety Directorate of the Republic of Croatia. Lung biodistribution studies performed by Artimmune were in compliance with French decree No. 2013-118 of February 1st 2013 on the protection of animals according with the Artimmune/CNRS Orleans animal facility accreditation for experimentation (N°F-45-234-006) for PK project accreditation for experimentation (CLE-CECCO-2013; ApaFis#25609) and approved by the French Ministry of Agriculture for experiments with laboratory animals (law 87-848). Rat PK studies at Labcorp were performed according to the United Kingdom Animals (Scientific Procedures) Act 1986 (Amendment Regulations 2012) and approved by the Animals in Science Regulation Unit (ASRU) of the UK Home Office. Studies in the silica-induced fibrosis model in mice were performed at Aragen under the Aragen IACUC approved protocol 22-0325-MR titled "Non-GLP Study: Efficacy Evaluation of Test Compounds in Crystalline Silicon Oxide-induced Lung Fibrosis in Rodents"

Reporting of all animal studies was conducted in accordance with ARRIVE guidelines.

Materials

PRS-220 (WO2022214649A1, Seq ID 23) was manufactured by WuXi Biologics (Suzhou, China) if not stated differently. For all in vivo and ex vivo studies PRS-220 was diluted in its specific preclinical formulation buffer containing histidine, sucrose, D-mannitol, L-arginine monohydrochloride, sodium chloride and polysorbate 80. Pamrevlumab was produced internally using patent sequences (WO2004108764, Seq ID 14 & 20) and was formulated in PBS.

PRS-220 specific polyclonal antibodies were generated by BioGenes via rabbit immunization. Alexa Fluor 647-labeled PRS-220 and pamrevlumab were generated in-house using Alexa Fluor™ 647 NHS-Ester (Succinimidylester, Invitrogen™ A20006) according to the manufacturer's instructions.

Identification of PRS-220 by phage display selection and high-throughput screening

A random phagemid library based on human NGAL with a combinatorial diversity of 1.3×10^{10} was prepared by concerted mutagenesis of multiple amino acid positions. Panning was performed against in-house biotinylated recombinant human CCN2 (R&D systems) and clones after 4 panning rounds were characterized in a high-throughput ELISA screening for specific target binding. Following further biophysical characterization, an intermediate candidate (Fig. 1a) for optimization was selected. A dedicated library was generated via partial mutagenesis and a further cycle of phage display selection and screening under more stringent conditions than the initial panning was performed. Optimized clones were thoroughly assessed for developability resulting in PRS-220.

SPR

An 8 K Biacore instrument was used for SPR experiments. Human CCN2 tagged with human Fc (Creative Biomart) was immobilized onto a CM5 Sensor Chip (Cytiva) at a concentration to allow for analyte signal intensities between 10 and 50 RU. PRS-220 and pamrevlumab were applied in running buffer (HBS-EP+ pH 7.4) at 25 °C at different concentrations to the CCN2 coupled and the reference flow cell. Applying a flow rate of 30 µL/min, the sample contact time was 180 s and dissociation time was 9000 s. Data were evaluated and calculated with Biacore Insight Evaluation Version 3.0 software. Double referencing was used. The 1:1 binding model was used to fit the raw data of PRS-220; the bivalent fit model was used for pamrevlumab.

ECLA

For the competition ECLA, pamrevlumab was directly immobilized to a 384-well Sector® Imager Standard microtiter plate (Meso Scale Discovery) while PRS-220 or pamrevlumab in titration series were incubated with a fixed concentration of biotinylated human CCN2 (R&D systems; biotinylated by Pieris Pharmaceuticals GmbH) as tracer. Bound biotinylated CCN2 was detected with Streptavidin-SulfoTag (Meso Scale Discovery, R32AB-1, 1 µg/mL) and an MSD Sector Imager S600. In addition, a standard curve of CCN2-Bio was prepared in assay buffer. A schematic representation of the assay format is given in Fig. 1d. Evaluation was performed with GraphPad Prism 9 software as follows: The standard curve was fitted using a 4-parameter logistic (4PL) nonlinear regression model with $1/Y^2$ as weighting factor and was used to calculate the amount of non-neutralized (free) CCN2-Bio in the competition assay. This concentration was plotted versus the concentrations of PRS-220 and pamrevlumab and IC_{50} values were calculated.

Nebulization testing for post-nebulized integrity

An investigational PARI eFlow® Nebulizer System (mesh type 30), or eFlow Nebulizer, was used to perform nebulization experiments with PRS-220. Protein solution was nebulized as triplicates. The nebulizer was connected in a horizontal position to 50 R glass vials and sealed with parafilm between the handpiece and the vial to collect the nebulized material. The collected nebulized material was subjected to further analysis.

Next generation cascade impactor (NGI) method

Aerodynamic particle size distribution determination using next generation cascade impactor (Copley Scientific) was performed according to ISO 27427:2020-02 Annex D. Because the generated aerosol had no large particles, a pre-separator was not necessary (in accordance with USP and Ph.Eur.). Aerodynamic particle size distribution was determined for three devices.

Breathing simulator

The delivered dose was determined using a breathing simulator according to the method described in European Pharmacopoeia Chapter 2.9.44. The breathing simulator generated a sinusoidal breathing pattern with a breathing frequency of 15 breaths per minute and an inhalation volume of 500 mL. Delivered dose was determined for three devices measured in duplicate.

Confocal analysis of mucus penetration and interaction

Human bronchial epithelial cells (ΔF508 homozygous) from three cystic fibrosis patients (Marsico Lung Institute Tissue Procurement and Cell Culture Core, University of North Carolina) were cultured at an air-liquid interface for ~4 wk. Cultures were allowed to accumulate mucus secretions for 5 d, then stained with 10 kDa Alexa Fluor 633-dextran (Thermo Fisher Scientific) and 25 nm FITC fluorescent microspheres (Thermo Fisher Scientific) to visualize the ASL (airway surface liquid) and mucus. Cultures were left 24 h for the ASL to normalize. Images of the ASL and mucus were then rapidly captured by XZ-confocal microscopy using a Leica SP8 confocal microscope with a ×63 glycerol lens before and after the addition of Alexa Fluor 647-labeled PRS-220 or mucus binding microspheres.

Quartz Crystal Microbalance with Dissipation (QCMD) monitoring

A semipurified, native mucus preparation containing mucin 5B (MUC5B) and interacting proteins was used for PRS-220-mucus/mucin interactions[69]. Briefly, semipurified MUC5B from the void of Sepharose CL-2B gel filtration chromatography was deposited on gold-coated quartz crystals as previously described[69,70]. Following the mucin deposition period, PRS-220 (10 μM) was introduced to the mucin layer, and changes in dissipation and frequency were monitored in real-time using Qtools software (QSense; Biolin Scientific). After system stabilization, a positively charged control peptide (Poly-L-lysine, 10 μM) was added, and changes in dissipation and frequency were monitored.

Pharmacokinetic analysis of PRS-220 and pamrevlumab in mice

Male C57BL/6 N mice (Charles River, 8–10 weeks of age) received a single dose of PRS-220 via oropharyngeal aspiration (OA) or pamrevlumab via intravenous bolus injection (both 100 μg/mouse). Terminal sampling of plasma, BALF, and lung tissue was performed after 1, 4, 8 and 24 h for PRS-220 and after 1, 8, 24 and 96 h for pamrevlumab ($n = 4$ animals/timepoint). After BALF collection lungs were homogenized in PBS pH 7.4 (Gibco) and cOmplete™ protease inhibitor (Roche) by Ultra-Turrax (IKA) and total protein concentration was adjusted to 5 mg/mL. Plasma was obtained from blood collected in lithium-heparin coated tubes. Total drug levels were analyzed using electrochemiluminescence based assays. 384-well Sector® Imager Standard plates (MSD) were coated with an anti-NGAL polyclonal antibody (BioGenes, custom production, 1 μg/mL) or an AffiniPure anti-human IgG F(ab')$_2$ fragment specific antibody (Jackson ImmunoResearch, 109-005-097, 1 μg/mL). Biotinylated anti-NGAL antibody (1 μg/mL) or Biotin-SP AffiniPure mouse anti-human IgG, F(ab')$_2$ fragment specific antibody (Jackson ImmunoResearch, 209-065-097, 1 μg/mL) and Streptavidin Sulfo-Tag (Meso Scale Discovery, R32AB-1, 1 μg/mL) were used for specific detection with an MSD Sector Imager S600 (Meso Scale Discovery). Exposure levels were determined using a standard curve in the linear range. A non-compartmental analysis was performed using Phoenix WinNonlin 8.3. Mice were housed at 22 ± 2 °C with normal lighting cycle (12 h light/dark) and a relative humidity of 55 ± 10%.

Fluorescence imaging of PRS-220 and pamrevlumab in healthy mouse lungs

Female C57BL/6 J mice (Janvier, 9 weeks of age) were treated with Alexa Flour 647 labeled PRS-220 via oropharyngeal aspiration or intravenously delivered Alexa Fluor 647-labeled pamrevlumab (both 100 μg/mouse). After 2 h, lungs were fixed with 4% PFA for 24 h and embedded into paraffin. Tissue sections stained with DAPI were imaged at compound specific wavelength using an Axio Observer Z7 fluorescence microscope with Plan Apochromat 20X/0.8 objectives and Orca Flash 4 camera (Carl Zeiss). Experiment was performed with $n = 4$ mice per treatment group. Mice were housed at 22 ± 1.5 °C with normal lighting cycle (12 h light/dark) and a relative humidity of 50 ± 25 %.

3D lung biodistribution analysis in whole left bleomycin challenged lungs

Male C57BL/6 N mice (Charles River, 8 weeks of age) were treated with 1 mg/kg bleomycin (Enzo Life Sciences) by intranasal delivery. At Day 21 after bleomycin challenge mice were either treated with Alexa Fluor 647 labeled PRS-220 or vehicle control via oropharyngeal aspiration and intravenously delivered Alexa Flour 647-labeled pamrevlumab (both 100 μg/mouse). After 2, 8 and 24 h of treatment, lungs were fixed in situ with a closed chest cavity by perfusion through the trachea with 10% neutral buffered formalin (NBF) at a constant fluid pressure of 4.5 mL/min for 5 min using a NE-4000 syringe pump and kept overnight in 10% NBF at room temperature (RT). After clearing in dibenzyl ether, whole left lung lobes were 3D light sheet imaged using Ultramicroscope II (Miltenyi Biotec GmbH, Bergisch Gladbach, Germany) with Zyla 4.2PCL10 sCMOS camera (Andor Technology, Belfast, UK), MV PLAPO 2XC (Olympus, Tokyo, Japan) objective and SuperK EXTREME supercontinuum white-light laser EXR-15 (NKT Photonics, Birkerød, Denmark) at compound specific wavelength (630 nm excitation channel) and 560 nm excitation channel to visualize tissue autofluorescence. Compound fluorescence was quantified. Deep learning was used to locate fibrotic regions based on the autofluorescence channel of the scans. U-net network architecture[71] was used to create a 2D U-net with four repeated layers for encoding and four repeated layers for decoding, implemented in Python using the Keras machine learning library (https://github.com/keras-team/keras). To define compound-specific fluorescence spectral unmixing was performed to minimize the contribution of tissue autofluorescence in the acquired compound signals. The estimated autofluorescence contribution in the specific channel was calculated and removed based on ratios of voxel intensities between selected voxels in the autofluorescence channel and the corresponding voxels in the compound specific channel. Experiment was performed with $n = 6$ animals in the vehicle control group and $n = 3$ animals per timepoint for other treatment groups. Mice were housed at 22 ± 2 °C with normal lighting cycle (12 h light/dark) and a relative humidity of 55 ± 10%.

Inhaled PK study in rats

RccHanTM:WIST rats (male and female in a 1:1 ratio, 8–9 weeks of age) received PRS-220 via nose-only inhalation with an exposure of 2 h per day on 4 consecutive days at target dose levels of 5, 15.8 and 50 mg/kg/day or via a single, systemic administration via intravenous (IV) bolus at a dose of 2 mg/kg. Serum samples of the inhalation groups were collected on Days 1 and 4 immediately after dosing and 2.5, 3, 4, 6, 8, 10, 14, and 24 h post start of inhalation and for the IV group on Day 1 immediately after dosing and 0.5, 1, 2, 4, 6, 8, 12, and 22 h after completion of dosing ($n = 3$ per sex/group/time point). Lung tissue was collected at 1, 6 and 22 h after completion of dosing. Lung homogenates were prepared as described above. Free PRS-220 drug levels were determined using ECLA. Microtiter plates coated with recombinant human CCN2 (R&D systems) were incubated with sample dilutions and bound PRS-220 was detected with a polyclonal anti-PRS-220 antibody (BioGenes, custom production, 1 μg/mL) and an anti-rabbit IgG Sulfo-Tag antibody (Meso Scale Discovery, 1 μg/L) using an MSD Sector Imager S600 for lung homogenate measurements or a MESO QuickPlex SQ 120 (Meso Scale Discovery) for serum measurements. Exposure levels were determined using a standard curve in the linear range. The calibration curve was fitted using a 4-Parameter Logistic nonlinear regression model applying a weighting factor of $1/Y^2$ and used to calculate the concentrations of the tested samples. Non-compartmental analysis was applied to the data of free PRS-220 concentration in serum. No differences were observed between male and female animals with sex differences in dose-normalized Cmax and AUC

being <2-fold. Rats were housed at 20–24 °C with normal lighting cycle (12 h light/dark) and a relative humidity of 40–70%.

Silica-induced lung fibrosis mouse model

Male C57BL/6 mice (Taconic, 8 weeks of age) were instilled oropharyngeally with 100 mg/kg silica (Sigma) or saline. For PK analysis, healthy and silica challenged mice at Day 41 received a single treatment with PRS-220 (targeted delivered dose: 0.2, 1 and 5 mg/kg) via nose-only inhalation using a Buxco® Inhalation Tower. PRS-220 exposure in lung tissue and plasma was analyzed 0.25, 1, 2 (only plasma), 4, 8, and 24 h post treatment as described above ($n = 4$ mice/group/timepoint). For lung biodistribution analysis, $n = 4$ mice were treated with PRS-220 (targeted delivered dose: 5 mg/kg) by nose-only inhalation at Day 41 after silica challenge 2 h after administration, lungs were fixed in 10% NBF for 24 h and imaged as described below. For analysis of in vivo efficacy, silica challenged mice were either treated daily with PRS-220 (targeted delivered dose 5 mg/kg) or vehicle via nose-only inhalation, or with pamrevlumab (10 mg/kg) or vehicle every other day by intraperitoneal injection from Day 2 onwards. The dose of pamrevlumab was selected based on PK studies and published data[27]. At Day 42 after silica challenge, lung weights were recorded, and lung tissues were processed for hydroxyproline measurement according to the manufacturer's instructions (Sigma Hydroxyproline Kit MAK-008). Absorbance was measured at 560 nm and amount of hydroxyproline was calculated per lung. The in vivo efficacy was assessed in two independent studies with $n = 3$–6 mice/treatment group in the pilot and $n = 12$ mice/treatment group in the confirmatory study showing the same outcome. Animals were housed in a temperature-controlled room (permissible range: 18-24 °C) with a 12 h light/dark cycle and relative humidity of 55 ± 10%.

Fluorescence imaging of silica-challenged mouse lungs

Tissue sections were dewaxed, rehydrated, subjected to heat-induced antigen retrieval in citrate buffer (pH6, Vector Lab) for 20 min and blocked in 5% BSA at RT for 30 min. Sections were incubated with antibodies targeting PRS-220 (BioGenes, custom production) and antibodies against CCN2 (Biorbyt, orb422483, 5 μg/mL), CC10 (Santa Cruz; sc-365992, clone E-11, 2 μg/mL), and αSMA (Thermo Fisher eBioscience, 14-9760-82, clone 1A4, 5 μg/mL) in PBS containing 0.05% Tween-20 overnight at 4 °C. Alexa Fluor 647- and 488-labeled anti-IgG antibodies (Jackson Immuno Research, 711-605-152 at 5 μg/mL and Thermo Fisher Scientific Invitrogen A32849 at 5 μg/mL and A11001 at 10 μg/mL) were incubated in PBS containing 0.05% Tween-20 and DAPI (1 μg/mL) for 1 h at RT. Sections were mounted (Prolong Antifade Gold) imaged with the Leica THUNDER Imager Live Cell and 3D Assay and the Leica Application Suite X software. For image deconvolution, single images were processed with the Leica THUNDER Large Volume Computational Clearing.

Gene expression analysis by quantitative polymerase chain reaction (qPCR)

Post caval lung lobes were used for gene expression analysis. Qiagen RNeasy Plus Mini Kit (50) Cat. No. / ID: 74134 was used for RNA extraction. Post caval lobe tissue in Buffer RLT was lysed in 2.0 mL conical tubes containing 2.8 mm stainless steel grinding balls via Mini Beadbeater 16 (Biospec Products). Total RNA was isolated via RNeasy Kit (Qiagen): Total RNA was evaluated via NanoDrop One (Thermo Scientific). 1 μg of total RNA was used to generate cDNA via iScript Reverse Transcription Supermix for RT-qPCR (Bio-Rad). RT2 Qiagen primers were used for Timp1 and Ccl2. qPCR was conducted with 4 mL of 10X diluted cDNA using SsoAdvanced Universal SYBR Green Supermix (Bio-Rad) on a CFX96 (Bio-Rad). PCR products were evaluated via end point melt curve analysis to evaluate fidelity of PCR amplification. Gene expression profiles were generated using CFX Maestro software (Bio-Rad) with Rn18s (18S ribosomal RNA) serving as reference gene. Data are presented as RQ (Relative Quantification) values ($=2^{-\Delta\Delta Ct}$).

CCN2 immunohistochemistry in IPF lung tissues

This study protocol was consistent with the Research Code of the University Medical Center Groningen and the national ethical and professional guidelines ("Code of conduct for Health Research"). Human lung tissues used in this study were derived from leftover lung material after lung surgery, for tumor resection or lung transplantation, from archival materials that are exempt from consent in compliance with applicable laws and regulations (Dutch laws: Medical Treatment Agreement Act (WGBO) art 458 / GDPR art 9/ UAVG art 24). This material was not subject to the Medical Research Human Subjects Act in the Netherlands, and, therefore, an ethics waiver was provided by the Medical Ethical Committee of the University Medical Center Groningen. IPF lung tissue sections from $n = 16$ organ donors (9 male IPF donors, 6 female IPF donors, 1 undetermined) were deparaffinized followed by antigen retrieval in citrate buffer for 15 min. Endogenic peroxidase was blocked for 30 min in PBS containing 0.03% hydrogen peroxide. After washing with PBS, slides were incubated with an anti-CCN2 antibody (Abcam, ab6992, 0.625 μg/mL) overnight at 4 °C. Polyclonal goat anti-rabbit immunoglobulins labeled with HRP (Dako, P0448, 1 μg/mL) were applied for 45 min at RT. NovaRed was used for visualization and hematoxylin was used as a counterstain. Images were captured using a slide scanner (Hamamatsu Photonics) and the CCN2 expression profile was analyzed by a lung pathologist.

Ex vivo lung perfusion and fluorescence imaging

Human donor lungs ($n = 3$, 2 female and 1 male donor) declined for transplantation were obtained from the local organ-procurement organization (Center for Organ Recovery & Education) approved by the Center for Organ Research Involving Decedents (CORID) at the University of Pittsburgh. Informed consent was obtained from all donors in accordance to ethical guidelines and institutional protocols. The technique of normothermic ex vivo lung perfusion (EVLP) has been described previously[72,73]. After securing the endotracheal tube, lungs underwent a recruitment procedure followed by maintenance on volume control ventilation with lung protective volumes (6cc/kg of ideal body weight). Lungs were perfused for 4 h with STEEN solution™ (XVIVO). 20 min following the start of perfusion, 6.4 mg of Alexa Fluor 647-labeled PRS-220 was administered via nebulization with an InnoSpire Go portable mesh nebulizer (Philips) set up in-line with the mechanical ventilator circuit (Supplementary Fig. 3a). Peripheral wedge biopsies were obtained prior to drug administration, and at 2 h and 4 h. Perfusate (0, 1, 2, 3, and 4 h) and BALF (4 h) were sampled at 4 h. Lung biopsies underwent fixation with Zinc Formalin Fixative (Millipore Sigma) for imaging analysis[72]. Slides were de-paraffinized before antigen retrieval (Target retrieval solution, citrate pH 6, Agilent, Dako) in a pressure cooker at 105 °C for 20 min. Slides were rinsed with 0.01 M Tris, 0.15 M NaCl and 0.05% Tween 20 and incubated in 300 mM glycine for 30 min. Lung sections were blocked (Duolink blocking solution, Sigma) and incubated with the primary antibodies against CCN2 (Novus Biologicals, NB100-724, 5 μg/mL), smooth muscle actin (Santa Cruz, sc-53142, 1 μg/mL), PDGFR-alpha (Santa Cruz, sc-398206, clone B4, 2 μg/mL) and keratin-5 (BioLegend, 905901, 1 μg/mL) overnight at 4°C followed by fluorescent tag secondary antibodies plus DAPI (Biotium) for 1 h at RT. Slides were mounted (Fluoroshield mounting media, Abcam). Images were taken at 20x using an IX83 Olympus microscope.

In silico model for pulmonary drug delivery

A recently proposed and validated approach to simulate pulmonary drug delivery was used to predict the aerosol deposition in healthy and IPF lungs[57]. The underlying in silico model is a comprehensive and subject-specific representation of the whole human lung, including all

conducting airways and the entire alveolar tissue (healthy and diseased). It enables computer simulations of airflow, local tissue deformation, particle transport and deposition throughout the whole lung with an unprecedented spatial and temporal resolution. Another advantage of this novel approach is the ability to simulate the exhalation phase and to use time-dependent aerosol characteristics.

Three individuals were selected for the in silico inhalation study to cover the range from a healthy lung over mild IPF to severe IPF. The healthy case (male, age 20 years) was taken from a data set published for the purpose of model validation[74], whereas the two IPF cases (1 female subject age 69 years, 1 male subject age 85 years) were selected from the OSIC data repository[75]. A standard breathing pattern with sinusoidal flow curve (500 mL tidal volume, 15 breaths/min, 1:1 inspiration/expiration ratio) was used for all cases. The aerosol characteristics were chosen in accordance with nebulizer characterization experiments according to USP guidelines and used for all cases. More information on the subject-specific model generation and the simulation setup is provided in Supplementary Table 4 and 5. More information on the method is provided in the supplementary information.

Generation of subject-specific in silico models

The process of subject-specific model generation started with the segmentation of airways, lungs, lobes, and fibrotic tissue from a high-resolution CT scan (Fig. 6a). Based on the extracted volumetric information and a physiology-based, space-filing growth algorithm, the full 16-generation tree of conducting airways and alveolar cluster units connected to terminal airways were generated (Fig. 6b). The material parameters of the model were calibrated individually for all three cases based on the available spirometry and physiological data (Supplementary Table 4 and 5). In addition, the effect of fibrotic tissue was modeled by a 5-fold higher tissue stiffness and viscosity in the segmented, severely fibrotic regions (Supplementary Table 6 and visualized in Fig. 6a) and an adjustment of the tissue stiffness and viscosity with the local radiodensity of the lung tissue from the CT scan in the remaining parts of the lung.

Additional information about the simulation setup used in the in silico study

Specifically, a mass median aerodynamic diameter of 3.9 μm and a geometric standard deviation of 1.6 were used to define droplet size distribution in all cases. A time-dependent aerosol output rate (AOR) was used. The AOR was linearly interpolated between given values 500 mg/min at time $t = 0$ s, 200 mg/min at time $t = 0.8$ s, and 0 mg/min throughout the exhalation phase $2\,s < t < 4$ s. For computational feasibility, the inhaled aerosol mass was reduced by a constant factor that led to a total number of about 500,000 particles per case. It was ensured that any further increase of the particle count beyond about 100,000 particles had no considerable effect on the deposition statistics evaluated in this study. These deposition statistics, such as the mass fraction of aerosol deposited in the conducting airways or in the alveolar tissue, were evaluated by leveraging the single particle resolution and tracking of the modeling approach that allows for a detailed analysis of the spatial distribution of deposited particles throughout the whole lung.

Human IPF PCLS

Explanted lungs were obtained from the Department of Thoracic Surgery, Vienna. The study protocol was approved by the Ethics Committee of the Justus-Liebig-University School of Medicine (111/08 and 58/15). Informed consent was obtained from all donors in accordance to ethical guidelines and institutional protocols. The data and all patient-related biomaterials used for the PCLS experiment were provided by the UGMLC Giessen Biobank and the European IPF Registry/Biobank. All IPF diagnoses were made according to the American Thoracic Society/European Respiratory Society consensus criteria. Precision cut lung slices (PCLS) were performed from explanted lungs from 3 patients with IPF (2 female, 1 male donors). In histopathological sections of the explanted lungs, a usual interstitial pneumonia (UIP) pattern was re-confirmed. PCLS were performed and cultured as described previously[63,64]. Briefly, 1.5% – 3% low melting agarose (maintained at 37 °C) was filled in each segment of explanted human IPF lung and was allowed to cool on ice for 30 min for the agarose to solidify. Vibrating blade microtome (Thermo Fisher) was used to section blocks. 500 μm thick sections were made and were cultured in RPMI medium without phenol red supplemented with 2% FCS, 1% penicillin / streptomycin and 1% L-Glutamine. PCLS were left for 24–48 h in cell culture incubator. Before treatments, PCLS were washed with PBS. PCLS were treated with PRS-220 (100 nM & 500 nM), pamrevlumab (100 nM), nintedanib (2 μM), or Vehicle (Veh) every day. Treated PCLS were harvested on day 5 by shock freezing. Total protein lysates were then prepared and western blot for COL1A1 (R&D Systems, AF6220, 1 μg/mL) or GAPDH (Cell Signaling, 2118, clone 14C10, 1:1000) were performed using standard protocols. $N = 4–5$ PCLS per treatment group were used from each patient lung. Uncropped blots are provided in the Source Data file.

ELISA

Recombinant protein of CCN2, its N- and C-terminal fragment or other CCN family members (various suppliers) were coated onto microtiter plates and incubated with a titration series of PRS-220. Binding was detected using a peroxidase-conjugated anti-NGAL antibody (BioGenes, custom production) and a fluorogenic substrate (QuantaBlu). Fluorescence intensity was plotted against the concentration of the test item. The data were fit with a 4PL fit model. The EC_{50} values were used to compare the binding properties to the different targets.

NHLF binding assay

PRS-220 binding to CCN2 expressed by TGF-β1 activated primary normal human lung fibroblasts (NHLF) in vitro was assessed in "scar-in-a-jar" assay[76]. NHLF (Lonza) were seeded in 96-well plates in FGM-2 medium with FGMTM-2 SingleQuotsTM supplements (Lonza) and 0.4 % FBS (Sigma). After 24 h medium was replaced by FGM-2 medium with 0.4% FBS, 50 μg/ml L-Ascorbic acid, 37.5 mg/mL Ficoll PM70 and 25 mg/mL Ficoll PM400 (all Sigma). Cells were treated with 5 ng/mL TGF-β1 (R&D Systems) and PRS-220 or respective Anticalin scaffold for 24 h. Cells were fixed in 4% PFA, blocked with 5% BSA in PBS, and stained with 10 μg/mL Alexa Fluor 647-labeled polyclonal anti-NGAL antibody (BioGenes, custom production) and DAPI (Invitrogen) for 1 h at RT. Imaging was performed using the Cytation 5 Imager with LED cubes at respective wavelength and Gen 5 Image Prime Software (Agilent). Staining intensities were quantified and normalized to DAPI and background. Results of three independent experiments with $n = 3$ technical replicates/condition are shown.

Light obscuration (LO)

Microparticle analysis was performed using LO with the HIAC 9703b (Beckman-Coulter) instrument. Samples were generally run as is. A water wash protocol was used after each analysis, and the number of microparticles measured in "particle-free" water before each subsequent run was generally <10 particles/mL. For each sample the standard deviation and mean were calculated from the values of last 3 of the 4 sample draws.

Turbidity measurements

Turbidity was determined with a CLARIOstarPlus (BMG labtech) Plate Reader. The formazin solution (4000 NTU) was diluted to 0, 3, 6, 18, 30, and 60 NTU in water in order create a calibration curve. The absorption of samples and formazin standards was measured in a wavelength scan from 500 to 600 nm in 1 nm increment. The measured absorbance values were normalized into NTU based on the

calibration curve, and the average calculated. After subtraction of the normalized turbidity of the solvent, the average normalized turbidity for two replicates and the standard deviation were calculated and reported.

cIEF

The cIEF measurements were performed on a Maurice system from Protein Simple. The separation mix (1% methylcellulose—Protein Simple, 20% SimpleSol®—Protein Simple, 2% Pharmalytes® pH 3-10 – Sigma Aldrich, 2% Pharmalytes® pH 8.0-10.5 – Sigma Aldrich, 2% pI markers 7.05 and 10.17, 10 mM arginine, and desalted sample (final concentration: 0.025 mg/ml)) was centrifuged at 10,000 x g for 3 min, separated (1 min 1500 Volts, 10 min 3000 Volts) and measured by fluorescence detection.

SEC

The SEC analytic was performed on an HPLC using an XBridge Protein BEH SEC Column (125 Å, 3.5 μm, 7.8 mm × 150 mm, SN 186007623, Waters) and an XBridge Protein BEH SEC Guard Column (125 Å, 3.5 μm, 7.8 mm × 30 mm, SN 186007635, Waters) with an isocratic separation (flowrate: 0.86 mL/min; running buffer: 150 mM sodium phosphate buffer, pH 7.0, column temperature: ambient) over 10 min. 10 μg sample (1 mg/mL, diluted with running buffer) was injected and evaluated at 280 nm.

nanoDSC

A nanoDSC with platinum capillaries from TA instruments (K20313) was used for melting point analysis. The thermal gradient in scanning mode ranged from 25 °C to 100 °C with an increment of 1 °C/min. During the measurements a constant pressure of 3 atm was applied. Samples were diluted to 1 mg/mL. For the modelling of the thermal data the two-state scaled model was used.

HPLC method for quantification of PRS-220

An isocratic HPLC method was used to measure recovery of PRS-220 in NGI and breathing simulator. 10 μL of PRS-220 were loaded on a BioResolve RP mAB Polyphenyl, 450 A, 2.7 μM 4.6 × 150 mm column (column temperature: 60 °C; sample temperature: 4 °C) and run over 6 min at a flow rate of 0.7 mL/min and with a mobile phase A to B ratio of 60/40 (0.1% TFA in HPLC water / Acetonitril v/v). Detection took place at UV 280 nm.

Binding Potency (ECLA)

Binding potency was determined by a qualified electrochemiluminescence assay (ECLA) where human CCN2 (R&D Systems) was coated and PRS-220 samples were detected with a polyclonal rabbit anti-PRS-220 antibody (BioGenes, custom production, 1 μg/mL) in combination with goat anti-rabbit IgG-SulfoTag (Meso Scale Discovery, R32AB-1, 1 μg/mL). Study samples had to be diluted into the linear range of the standard curve between the low- and high-quality control. One dilution for each initial concentration was prepared and analyzed along with calibration curve samples and two sets of quality control samples. All samples were analyzed in duplicates. Recoveries in % were calculated and represent the binding potency of PRS-220.

Statistics & Reproducibility

Statistical analysis was performed using Graphpad Prism version 10 (or 9 as described in the respective experiment). Non-compartmental PK analysis was performed using Phoenix WinNonlin 8.3. In vivo efficacy experiments were performed twice. Three independent experiments were conducted for in vitro and in ex vivo studies. Data were reproducible.

No statistical methods were used to predetermine sample sizes. For PK analysis in mice, we used $n = 4$ animals per timepoint/group. In PK studies in rats $n = 3$ per sex/group/time point was used. Lung biodistribution studies in healthy mice were performed with $n = 4$ mice per treatment group. Lung biodistribution studies in bleomycin challenged mice were performed with $n = 6$ in the vehicle group and $n = 3$ per timepoint for other treatment groups. In the silica-induced fibrosis model $n = 3$ - 6 mice/treatment group was used in the pilot and $n = 12$ mice/treatment group in the confirmatory study showing the same outcome. Sample sizes were determined to balance the use of animals, the study size with regard to handling and the robustness and reproducibility of the results. Animals were distributed into groups based on similar mean weight. The Investigators were not blinded to allocation during experiments and outcome assessment.

For experiments with human tissue, sample sizes were determined based on the availability of donor material. IPF lung tissue sections for immunohistochemistry from $n = 16$ organ donors were used. $N = 3$ whole human donor lungs were used for ex vivo lung perfusion studies. Lung tissue from $n = 3$ IPF patients were used for the PCLS study.

In the NHLF binding experiments single wells were excluded from analysis when they fulfilled one of the following criteria: (1) Technical problems with autofocus; (2) Wells with very high or very low cell count, outside of 98% Confidence Interval. (3) Software problems during picture processing

Reporting summary

Further information on research design is available in the Nature Portfolio Reporting Summary linked to this article.

Data availability

All data supporting the findings described in this manuscript are available within the paper and its Supplementary Information. Source data are provided within this paper. Source data are provided with this paper.

References

1. Rau, J. L. The inhalation of drugs: advantages and problems. *Res. Care* **50**, 367–382 (2005).
2. West, A. et al. Inhaled pirfenidone solution (AP01) for IPF: a randomised, open-label, dose–response trial. *Thorax* **78**, 882–889 (2023).
3. Cottin, V. & Maher, T. Long-term clinical and real-world experience with pirfenidone in the treatment of idiopathic pulmonary fibrosis. *Eur. Resp. Rev.* **24**, 58–64 (2015).
4. Anselmo, A. C., Gokarn, Y. & Mitragotri, S. Non-invasive delivery strategies for biologics. *Nat. Rev. Drug Discov.* **18**, 19–40 (2018).
5. Fröhlich, E. & Salar-Behzadi, S. Oral inhalation for delivery of proteins and peptides to the lungs. *Eur. J. Pharm. Biopharma.* **163**, 198–211 (2021).
6. Fröhlich, E. Biological obstacles for identifying in vitro-in vivo correlations of orally inhaled formulations. *Pharmaceutics* **11**, 316 (2019).
7. Hutchinson, J., Hubbard, R. & Raghu, G. Surgical lung biopsy for interstitial lung disease: when considered necessary, should these be done in larger and experienced centres only? *Eur. Resp. J.* **53**, 1900023 (2019).
8. Skerra, A. Alternative binding proteins: anticalins - harnessing the structural plasticity of the lipocalin ligand pocket to engineer novel binding activities. *FEBS J.* **275**, 2677–2683 (2008).
9. Richter, A., Eggenstein, E. & Skerra, A. Anticalins: Exploiting a non-Ig scaffold with hypervariable loops for the engineering of binding proteins. *FEBS Lett.* **588**, 213–218 (2014).
10. Rothe, C. & Skerra, A. Anticalin® proteins as therapeutic agents in human diseases. *BioDrugs* **32**, 233–243 (2018).
11. Morales-kastresana, A. et al. Anticalin ® -based therapeutics: expanding new frontiers in drug development. *Int. Rev. Cell Mol. Biol.* **369**, 89–106 (2022).

12. Matschiner, G. et al. Elarekibep (PRS-060/AZD1402), a new class of inhaled Anticalin medicine targeting IL-4Ra for type 2 endotype asthma. *J. Allergy Clin. Immunol.* **151**, 966–975 (2023).
13. Wynn, T. A. Integrating mechanisms of pulmonary fibrosis. *J. Exp. Med.* **208**, 1339–1350 (2011).
14. Maher, T. M. & Strek, M. E. Antifibrotic therapy for idiopathic pulmonary fibrosis: time to treat. *Resp. Res.* **20**, 205 (2019).
15. Perbal, B., Tweedie, S. & Bruford, E. The official unified nomenclature adopted by the HGNC calls for the use of the acronyms, CCN1–6, and discontinuation in the use of CYR61, CTGF, NOV and WISP 1–3 respectively. *J. Cell Commun. Signal.* **12**, 625–629 (2018).
16. Leask, A. Conjunction junction, what's the function? CCN proteins as targets in fibrosis and cancers. *Am. J. Physiol. Cell Physiol.* **318**, C1046–C1054 (2020).
17. Ramazani, Y. et al. Connective tissue growth factor (CTGF) from basics to clinics. *Matrix Biol.* **68–69**, 44–66 (2018).
18. Pan, L. H. et al. Type II alveolar epithelial cells and interstitial fibroblasts express connective tissue growth factor in IPF. *Eur. Resp. J.* **17**, 1220–1227 (2001).
19. Dorn, L. E., Petrosino, J. M., Wright, P. & Accornero, F. CTGF/CCN2 is an autocrine regulator of cardiac fibrosis. *J. Mol. Cell. Cardiol.* **121**, 205–211 (2018).
20. Rachfal, A. Connective tissue growth factor (CTGF/CCN2) in hepatic fibrosis. *Hepatol. Res.* **26**, 1–9 (2003).
21. Ito, Y. et al. Expression of connective tissue growth factor in human renal fibrosis. *Kidney Int.* **53**, 853–861 (1998).
22. Isshiki, T. et al. Therapeutic strategies to target connective tissue growth factor in fibrotic lung diseases. *Pharmacol. Ther.* **253**, 108578 (2024).
23. Klay, D. et al. Connective tissue growth factor single nucleotide polymorphisms in (Familial) pulmonary fibrosis and connective tissue disease associated interstitial. *Lung Dis. Lung* **199**, 659–666 (2021).
24. Yanagihara, T. et al. Connective-tissue growth factor contributes to TGF-β1–induced lung fibrosis. *Am. J. Resp. Cell Mol. Biol.* **66**, 260–270 (2022).
25. Bonniaud, P. et al. Adenoviral gene transfer of connective tissue growth factor in the lung induces transient fibrosis. *Am. J. Resp. Crit. Care Med.* **168**, 770–778 (2003).
26. Sonnylal, S. et al. Selective expression of connective tissue growth factor in fibroblasts in vivo promotes systemic tissue fibrosis. *Arthritis Rheumatism* **62**, 1523–1532 (2010).
27. Wang, Q. et al. Cooperative interaction of CTGF and TGF-β in animal models of fibrotic disease. *Fibrogenes. Tissue Repair* **4**, 1–11 (2011).
28. Parapuram, S. K. et al. Loss of PTEN expression by mouse fibroblasts results in lung fibrosis through a CCN2-dependent mechanism. *Matrix Biol.* **43**, 35–41 (2015).
29. Tam, A. Y. Y. et al. Selective deletion of connective tissue growth factor attenuates experimentally -induced pulmonary fibrosis and pulmonary arterial hypertension. *Int. J. Biochem. Cell Biol.* **134**, 105961 (2021).
30. Bickelhaupt, S. et al. Effects of CTGF blockade on attenuation and reversal of radiation-induced pulmonary fibrosis. *JNCI: J. Natl Cancer Inst.* **109**, 1–11 (2017).
31. Richeldi, L. et al. Pamrevlumab, an anti-connective tissue growth factor therapy, for idiopathic pulmonary fibrosis (PRAISE): a phase 2, randomised, double-blind, placebo-controlled trial. *Lancet Resp. Med.* **8**, 25–33 (2020).
32. Raghu, G. et al. Pamrevlumab for idiopathic pulmonary fibrosis. *JAMA* **332**, 380 (2024).
33. Tam, A. Y. Y. et al. Selective deletion of connective tissue growth factor attenuates experimentally-induced pulmonary fibrosis and pulmonary arterial hypertension. *Int. J. Biochem. Cell Biol.* **134**, 105961 (2021).
34. Sung, D. K. et al. Noncovalenly PEGylated CTGF siRNA/PDMAEMA complex for pulmonary treatment of bleomycin-induced lung fibrosis. *Biomaterials* **34**, 1261–1269 (2013).
35. George, J. & Tsutsumi, M. siRNA-mediated knockdown of connective tissue growth factor prevents N-nitrosodimethylamine-induced hepatic fibrosis in rats. *Gene Ther.* **14**, 790–803 (2007).
36. Kang, S. et al. RNAi nanotherapy for fibrosis: highly durable knockdown of CTGF/CCN-2 using siRNA-DegradaBALL (LEM-S401) to treat skin fibrotic diseases. *Nanoscale* **12**, 6385–6393 (2020).
37. Ren, Y. et al. CTGF siRNA ameliorates tubular cell apoptosis and tubulointerstitial fibrosis in obstructed mouse kidneys in a Sirt1-independent manner. *Drug Des., Dev. Ther.* **9**, 4155–4171 (2015).
38. Laube, B. L. et al. What the pulmonary specialist should know about the new inhalation therapies. *Eur. Resp. J.* **37**, 1308–1417 (2011).
39. Moore, B. B. & Hogaboam, C. M. Murine models of pulmonary fibrosis. *Am. J. Physiol. Lung Cell. Mol. Physiol.* **294**, L152–L160 (2008).
40. Lavorini, F., Buttini, F. & Usmani, O. S. 100 years of drug delivery to the lungs. *Handb. Exp. Pharmacol.* **260**, 143–159 (2019).
41. Spagnolo, P. et al. Shedding light on developmental drugs for idiopathic pulmonary fibrosis. *Expert Opin. Investig. Drugs* **29**, 797–808. (2020).
42. Nathan, S. D. et al. Study design and rationale for the TETON phase 3, randomised, controlled clinical trials of inhaled treprostinil in the treatment of idiopathic pulmonary fibrosis. *BMJ Open Resp. Res.* **9**, 1–6 (2022).
43. Hertel, S. P., Winter, G. & Friess, W. Protein stability in pulmonary drug delivery via nebulization. *Adv. Drug Deliv. Rev.* **93**, 79–94 (2015).
44. Mayor, A. et al. Inhaled antibodies: formulations require specific development to overcome instability due to nebulization. *Drug Deliv. Transl. Res.* **11**, 1625–1633 (2021).
45. Hickey, A. J., Stewart, I. E., Hickey, A. J. & Stewart, I. E. Inhaled antibodies: quality and performance considerations Inhaled antibodies: Quality and performance considerations ABSTRACT. *Hum. Vaccines Immunotherap.* **00**, 1–10 (2021).
46. Shah, D. K. & Betts, A. M. Antibody biodistribution coefficients. *mAbs* **5**, 297–305 (2013).
47. Hart, T. K. et al. Preclinical efficacy and safety of mepolizumab (SB-240563), a humanized monoclonal antibody to IL-5, in cynomolgus monkeys. *J. Allergy Clin. Immunol.* **108**, 250–257 (2001).
48. Magyarics, Z. et al. Randomized, double-blind, placebo-controlled, single-ascending-dose study of the penetration of a monoclonal antibody combination (ASN100) targeting staphylococcus aureus cytotoxins in the lung epithelial lining fluid of healthy volunteers. *Antimicrobial. Agents Chemother.* **63**, 1–13 (2019).
49. Dall'Acqua, W. F., Kiener, P. A. & Wu, H. Properties of human IgG1s engineered for enhanced binding to the neonatal Fc receptor (FcRn). *J. Biol. Chem.* **281**, 23514–23524 (2006).
50. Sadiq, M. W. et al. Lung pharmacokinetics of inhaled and systemic drugs: a clinical evaluation. *Br. J. Pharmacol.* **178**, 4440–4451 (2021).
51. Man, F., Tang, J., Swedrowska, M., Forbes, B. & de Rosales, T. M. R. Imaging drug delivery to the lungs: Methods and applications in oncology. *Adv. Drug Deliv. Rev.* **192**, 114641 (2023).
52. Scheuch, G. et al. Deposition, imaging, and clearance: What remains to be done? *J. Aerosol Med. Pulm. Drug Deliv.* **23**, S39–57 (2010).
53. Gnadt, M. et al. Methacholine delays pulmonary absorption of inhaled β2-agonists due to competition for organic cation/carnitine transporters. *Pulm. Pharmacol. Therap.* **25**, 124–134 (2012).
54. Freiwald, M. et al. Monitoring the initial pulmonary absorption of two different beclomethasone dipropionate aerosols employing a human lung reperfusion model. *Resp. Res.* **6**, 1–13 (2005).
55. Mürdter, T. E. et al. Dose optimization of a doxorubicin prodrug (HMR 1826) in isolated perfused human lungs: low tumor pH

promotes prodrug activation by β-glucuronidase. *J. Pharmacol. Exp. Therap.* **301**, 223–228 (2002).
56. Ku, T. J. Y. et al. Ex-vivo delivery of monoclonal antibody (Rituximab) to treat human donor lungs prior to transplantation. *EBioMedicine* **60**, 102994 (2020).
57. Grill, M. J. et al. In silico high-resolution whole lung model to predict the locally delivered dose of inhaled drugs. *arXiv* https://doi.org/10.48550/arXiv.2307.04757 (2023).
58. Usmani, O. S. et al. The topical study of inhaled drug (salbutamol) delivery in idiopathic pulmonary fibrosis. *Resp. Res.* **19**, 1–10 (2018).
59. Maher, T. M. et al. A positron emission tomography imaging study to confirm target engagement in the lungs of patients with idiopathic pulmonary fibrosis following a single dose of a novel inhaled αvβ6 integrin inhibitor. *Resp. Res.* **21**, 1–9 (2020).
60. Spagnolo, P. & Maher, T. M. Clinical trial research in focus: why do so many clinical trials fail in IPF? *Lancet Resp. Med.* **5**, 372–374 (2017).
61. Blackwell, T. S. et al. Future directions in idiopathic pulmonary fibrosis research an NHLBI workshop report. *Am. J. Resp. Crit. Care Med.* **189**, 214–222 (2014).
62. Jenkins, R. G. et al. An official American thoracic society workshop report: use of animal models for the preclinical assessment of potential therapies for pulmonary fibrosis. *Am. J. Respir. Cell Mol. Biol.* **56**, 667–679 (2017).
63. Yanagihara, T. et al. Current models of pulmonary fibrosis for future drug discovery efforts. *Expert Opin. Drug Discov.* **15**, 931–941 (2020).
64. Hesse, C. et al. Nintedanib modulates type III collagen turnover in viable precision-cut lung slices from bleomycin-treated rats and patients with pulmonary fibrosis. *Resp. Res.* **23**, 1–9 (2022).
65. Decaris, M. L. et al. Dual inhibition of αvβ6 and αvβ1 reduces fibrogenesis in lung tissue explants from patients with IPF. *Resp. Res.* **22**, 1–14 (2021).
66. Wollin, L., Maillet, I., Quesniaux, V., Holweg, A. & Ryffel, B. Antifibrotic and anti-inflammatory activity of the Tyrosine Kinase inhibitor Nintedanib in experimental models of lung fibrosiss. *J. Pharmacol. Exp. Ther.* **349**, 209–220 (2014).
67. Guo, J. et al. Pirfenidone inhibits epithelial-mesenchymal transition and pulmonary fibrosis in the rat silicosis model. *Toxicol. Lett.* **300**, 59–66 (2019).
68. Raghu, G. et al. Efficacy of simtuzumab versus placebo in patients with idiopathic pulmonary fibrosis: a randomised, double-blind, controlled, phase 2 trial. *Lancet Res. Med.* **5**, 22–32 (2017).
69. Radicioni, G. et al. The innate immune properties of airway mucosal surfaces are regulated by dynamic interactions between mucins and interacting proteins: the mucin interactome. *Mucosal Immunol.* **9**, 1442–1454 (2016).
70. Kesimer, M. & Sheehan, J. K. Analyzing the functions of large glycoconjugates through the dissipative properties of their absorbed layers using the gel-forming mucin MUC5B as an example. *Glycobiology* **18**, 463–472 (2008).
71. Ronneberger, O., Fischer, P. & Brox, T. U-Net: Convolutional networks for biomedical image segmentation. In *Medical Image Computing and Computer-Assisted Intervention -- MICCAI 2015* (eds. Navab, N., Hornegger, J., Wells, W. M. & Frangi, A. F.) 234–241 (Springer International Publishing, 2015).
72. Snyder, M. E. et al. Human lung-resident macrophages colocalize with and provide costimulation to PD1hi tissue-resident memory T cells. *Am. J. Resp. Crit. Care Med.* **203**, 1230–1244 (2021).
73. Weathington, N. M. et al. Ex vivo lung perfusion as a human platform for preclinical small molecule testing. *JCI Insight* **3**, 1–12 (2018).
74. Conway, J. et al. Controlled, parametric, individualized, 2-D and 3-D imaging measurements of aerosol deposition in the respiratory tract of healthy human subjects for model validation. *J. Aerosol. Sci.* **52**, 1–17 (2012).
75. Open Source Imaging Consortium (OSIC). *OSIC Cloud Data Repository*. https://www.osicild.org/dr-about.html (2025).
76. Good, R. B. et al. A high content, phenotypic 'scar-in-a-jar' assay for rapid quantification of collagen fibrillogenesis using disease-derived pulmonary fibroblasts. *BMC Biomed. Eng.* **1**, 1–10 (2019).

Acknowledgements

Funding was provided by a grant from the Bavarian Ministry of Economic Affairs, Regional Development and Energy within the framework of the Bavarian Therapy Strategy to combat the COVID-19 pandemic ("Bay-Therapie2020"). Part of the work was supported by NIH grant R01 HL146519 to O.E. We would like to thank Urmas Roostalu and the team at Gubra for generating the light sheet microscopy data. We would also like to thank the team at Artimmune for generating the lung biodistribution data in healthy mice. Studies in the silica-induced fibrosis model were conducted at Aragen Life Sciences, with special thanks to Rashmi Munshi and Malavika Ghosh. In-life studies in the bleomycin-induced mouse model were performed at Fidelta, and we also thank Ines Glojnaric and Hrvoje Brzica from the Fidelta team for their contributions. Nebulization data if not stated differently were generated using the e-flow Nebulizer System from PARI Pharma GmbH. We would like to especially thank the scientists and research assistants at Pieris Pharmaceuticals who conducted important experiments that contributed to this work: David Goricanec, Patrizia Schneider, Patrick Zägel, Alexander Hahn, Mareike Maurer, Christina Hechinger, Nicolas Quilitz, Sarah Schmalbrock, and Adam Cichy. We would also like to thank Marie Brei, Jakob Richter, and Maximilian Rixner for their valuable contributions to the in silico experiments conducted by Ebenbuild.

Author contributions

V.N. identified preclinical models, led and supervised preclinical studies and designed experiments. M.P. supervised and supported the design of experiments. M.P. and V.N. provided overall strategy, interpreted data, and wrote the main parts of the manuscript. M.F.F., G.M., and S.A.O. provided strategical input, contributed to the design and supervision of the work as well as the interpretation of data. M.F.F., G.M., S.A.O., E.M.H., V.N., M.P., J.K.P., M.J.G., J.B., K.W.M., K.R.W., M.E.S., A.E., O.E., P.M., A.G., Co.W., N.S., S.G. and J.K.B. reviewed the manuscript. E.M.H. supervised, evaluated and provided data interpretation for binding experiments and PK analysis and gave strategic input. T.J. and A.F. coordinated and evaluated in vivo efficacy and lung biodistribution experiment in mice and contributed to data interpretation. J.K.P. designed and supervised in vitro and ex vivo experiments, provided data interpretation and drafted graphical schemes depicted in the manuscript. M.J.G., J.B., K.W.M. and K.R.W. designed and performed the in silico experiments and wrote parts of the manuscript. M.E.S., A.E., K.N. and O.E. designed, performed and provided data interpretation to the ex vivo lung perfusion studies. P.M., K.Ho. and A.G. designed, performed and provided data interpretation to the ex vivo PCLS studies. Co.W. designed, supervised and evaluated PK experiments. A.K. provided PRS-220 material to conduct animal experiments and designed, supervised and evaluated the nebulization studies. K.H. designed, supervised and evaluated in vitro and mouse lung imaging experiments. S.K. performed and evaluated mouse lung imaging experiments. N.S. designed, performed and evaluated the nebulization studies. S.G. drove protein engineering and designed the maturation strategy to obtain the PRS-220 drug candidate. D.B. performed and evaluated mouse lung imaging experiments. T.M. performed and evaluated binding experiments and analyzed PK samples. J.W. and R.T. designed, performed and evaluated the mucus interaction experiments. M.R. designed and evaluated the analysis of PK samples. J.K.B. designed, supervised and evaluated CCN2 immunohistochemistry experiments in IPF lungs. Cl.W. and G.M. supervised and designed panning and optimization experiments that led to the selection of the PRS-220 drug candidate.

Competing interests

M.P., V.N., E.M.H., Cl.W., T.J., S.G., G.M. are co-inventors of an international patent filed by Pieris Pharmaceuticals on the CCN2-targeting Anticalin protein described in this manuscript (WO2022214649A1). V.N., E.M.H, T.J., J.K.G., Co.W., A.K., K.H., A.F., N.S., S.G., D.B., T.M., S.K., M.R., Cl.W., M.F.F., S.A.O., G.M. and M.P. are or were employees of Pieris Pharmaceuticals and may hold stock interests in Pieris Pharmaceuticals. M.J.G, K.R.W, J.B. and K.W.M are employees and/or shareholders of Ebenbuild GmbH and co-inventors on a pending patent application. J.K.B receives research funds from Boehringer Ingelheim. The remaining authors declare no competing interests.

Additional information

Supplementary information The online version contains supplementary material available at https://doi.org/10.1038/s41467-025-58568-x.

Correspondence and requests for materials should be addressed to Marina Pavlidou.

Peer review information *Nature Communications* thanks Arne Skerra, and the other, anonymous, reviewer(s) for their contribution to the peer review of this work. A peer review file is available.

[1]Pieris Pharmaceuticals GmbH, 85399 Hallbergmoos, Germany. [2]Department of Internal Medicine, Justus Liebig University (JLU) Giessen, 35392 Giessen, Germany. [3]Universities of Giessen and Marburg Lung Center (UGMLC), Member of the German Center for Lung Research (DZL), Justus Liebig University, 35392 Giessen, Germany. [4]Department of Medicine, University of Pittsburgh, Pittsburgh, PA 15213, USA. [5]Department of Immunology, University of Pittsburgh, Pittsburgh, PA 15213, USA. [6]Starzl Transplantation Institute, Pittsburgh, PA 15213, USA. [7]Ebenbuild GmbH, 80469 Munich, Germany. [8]Division of Pulmonary, Allergy and Critical Care Medicine, University of Pittsburgh, Pittsburgh, PA 15213, USA. [9]University of North Carolina Department of Cell Biology & Physiology, Chapel Hill, NC 27599, USA. [10]Department of Cardiothoracic Surgery, University of Pittsburgh, Pittsburgh, PA 15213, USA. [11]Department of Thoracic Surgery Vienna, Medical University of Vienna, 1090 Vienna, Austria. [12]University of Groningen, University Medical Center Groningen, Department of Pathology and Medical Biology, 9713 GZ Groningen, the Netherlands. [13]University of Groningen, University Medical Center Groningen, Groningen Research Institute for Asthma and COPD (GRIAC), 9713 GZ Groningen, the Netherlands. [14]Agaplesion Evangelisches Krankenhaus Mittelhessen, 35398 Giessen, Germany. [15]European IPF Network and European IPF Registry, 35392 Giessen, Germany. [16]Member of the Cardio-Pulmonary Institute (CPI), Justus Liebig University Giessen, 35392 Giessen, Germany. [17]These authors contributed equally: Shane A. Olwill, Gabriele Matschiner, Marina Pavlidou. ✉e-mail: marinapavlidou5@gmail.com